

# 1 **Ground Motion Model for crustal events in Italy by applying the Multi-** 2 **Source Geographically Weighted Regression (MS-GWR) method**

3  
4 **Authors:** *Giovanni Lanzano<sup>1</sup>, Sara Sgobba, Luca Caramenti, Alessandra Menafoglio*

5  
6 <sup>1</sup>*corresponding author, email: giovanni.lanzano@ingv.it*

7 **The authors acknowledge there are no conflicts of interest recorded.**

## 8 9 **Abstract:**

10 In this paper, we implement a new approach to calibrate Ground Motion Models (GMMs)  
11 characterized by spatially varying coefficients, using the calibration dataset of an existing GMM  
12 for crustal events in Italy. The model is developed in the methodological framework of the Multi-  
13 Source Geographically-Weighted Regression (MS-GWR, Caramenti et al. 2020), which extends  
14 the theory of multiple linear regression to the case where the model coefficients are spatially  
15 varying, thus allowing to capture the multiple sources of non-stationarity in ground motion related  
16 to event and station locations. In this way, we reach the aim of regionalizing the ground motion in  
17 Italy, specializing the model in a non-ergodic framework. Such an attempt of regionalization also  
18 addresses the purpose to capture the regional effects in the modelling, which is a need for the  
19 Italian country, where ground-motion properties vary significantly across space. As the proposed  
20 model relies on the ITA18 (Lanzano et al., 2019) dataset and functional form, it could be  
21 considered as the ITA18 non-stationary version, thus allowing one to predict peak ground  
22 acceleration and velocity, as well as 36 ordinates of the 5%-damped acceleration response  
23 spectra in the period interval  $T=0.01-10s$ . The resulting MS-GWR model shows an improved  
24 ability to predict the ground motion locally, compared to stationary ITA18, leading to a significant  
25 reduction of the total variability at all periods, of about 15-20%. The paper also provides scenario-  
26 dependent uncertainties associated to the median predictions, to be used as a part of the  
27 epistemic uncertainty in the context of probabilistic seismic hazard analyses. Results show that  
28 the approach is promising to improve the model predictions especially on densely sampled areas,  
29 although further studies are necessary to resolve the observed trade-off inherent to site and path  
30 effects, which limits their physical interpretation.

## 1. Introduction

Ground Motion Models (GMM) are basic tools for the prediction of the seismic parameters adopted in many applications in engineering and seismology fields, such as the assessment of probabilistic and deterministic seismic hazard analysis and the definition of shaking scenarios. Basically, GMMs estimate the conditional distribution of the ground-motion parameters (median and associated standard deviation) given some explanatory variables, such as magnitude, distance, fault mechanism, proxies for site effects and other parameters. GMMs are commonly defined through closed-form and reproducible prediction equations, where several coefficients are derived by empirical regressions of strong motion parameters computed from datasets of recordings.

Before the 2000s, GMMs were mainly derived for relatively small areas where sufficient seismic records were available, such as California and Japan (see *Data and Resources* for the list of GMMs; a critical review of empirical GMMs can be found in Douglas & Edwards, 2016). These models were generally calibrated on datasets composed mainly of analog records of strong events. Although they often showed relatively small standard deviations, some strong motion parameters, such as long-period spectral acceleration ordinates, were poorly predicted, especially wherever suffering from waveforms filtering at low frequencies (Boore and Bommer, 2005). In Italy, the first GMM of Sabetta & Pugliese (1987,1996) represented the basis of the Italian seismic hazard map published in 2004 (MPS04, Stucchi et al. 2011).

Later on, the general trend in engineering seismology was to calibrate global GMMs encompassing very large areas over the continents, such as the pan-European GMMs (e.g., Bindi et al. 2014; Akkar et al. 2014). These global GMMs are typically based on the hypothesis of ergodicity, meaning that the distribution of ground motions over time at a given site is the same as their spatial distribution over all sites for the same magnitude, distance, and site condition (Anderson and Brune, 1999). Ergodic models thus provide shaking predictions even in areas where data are scarcely available, allowing the development of seismic hazard maps for vast areas (e.g., SHARE model, Woessner et al. 2015).

However, such an attempt to model the ground motion globally, caused a general increment of the standard deviations, as a result of the inclusion of earthquakes originating from different shallow active crustal regions, even from lower seismicity areas. Moreover, the absence of a proper regionalization in some models, results in predictions strongly influenced by the most sampled regions, e.g., the model by Cauzzi et al. (2015) which is Japan-biased and the model by Bindi et al. (2014) which is Italy-biased.

66 The regionalization was introduced for the first time in the NGA-West2 project (Bozorgnia et al.  
67 2014), where several global GMMs included regional corrective factors for site effects, mainly in  
68 terms of scaling with the shear-wave velocity, averaged in the uppermost 30 meters ( $V_{S,30}$ ), and  
69 anelastic attenuation in California, Taiwan, Japan, China and Italy (Abrahamson et al. 2014;  
70 Boore et al. 2014; Chiou and Youngs, 2014). Similar approaches were also carried out in Europe  
71 and Middle-East by Kotha et al. (2016, 2020), by including the regional dependence of apparent  
72 anelastic attenuation terms.

73 More recently, site-specific seismic hazard analyses for critical infrastructures (e.g., the  
74 PEGASOS study: Probabilistic Seismic Hazard Analysis for Swiss Nuclear Power Plant Sites)  
75 also showed that the ergodic approach leads to particularly severe estimates of the design  
76 spectral amplitudes, especially for longer return periods that are strongly affected by the standard  
77 deviation of the model (Cramer, 2003; Bazzurro and Cornell, 2004). To allow more accurate  
78 predictions of seismic motion and to reduce the associated variability, some methods have been  
79 introduced to move ergodic models into partially or totally non-ergodic models (Al Atik et al. 2010).  
80 In the practice, this goal is achieved by decomposing the model residuals into event and site  
81 terms (Rodriguez-Marek et al. 2011; Luzi et al. 2014), and more rarely also in source and path  
82 terms (Lin et al. 2011; Villani and Abrahamson, 2015; Lanzano et al. 2017), through the  
83 application of mixed-effects regression techniques (Stafford, 2014). In this way, the systematic  
84 sources of ground motion variability are recognized and accounted for as epistemic uncertainties,  
85 while reducing the aleatory component. Nevertheless, such corrections and the resulting  
86 reduction in variability are only beneficial for sites where seismic stations are installed, or for  
87 sources where significant earthquakes occurred.

88 In the last years, several efforts have been made to introduce the concepts of the geo-statistics  
89 into seismology with the aim to properly regionalize the ground motion and extend the benefits of  
90 the non-ergodic approach to sites where no records are available (Kuehn & Abrahamson, 2020;  
91 Schiappapietra & Douglas, 2020; Sgobba et al. 2019, 2021). The spatial regionalization is  
92 generally introduced in the ground motion modelling by means of two different approaches: 1) the  
93 first one consists in the calibration of spatial correlation models of the within-event residuals (Park  
94 et al., 2007; Goda and Atkinson, 2010; Esposito and Iervolino, 2012; Sokolov and Wenzel, 2011)  
95 and the repeatable site- and path- corrective terms (Anderson and Uchiyama, 2011; Sahakian et  
96 al., 2019; Kuehn and Abrahamson, 2020; Sgobba et al. 2019, 2021; Chao et al. 2020) to generate  
97 multiple realizations of ground-motion random fields; 2) the second way requires calibrating a  
98 model with spatially-variable regression coefficients, which provide a prediction model that is  
99 inherently non-ergodic (Landwehr et al., 2016). Considering that both the proposed approaches

100 allow one to remove (fully or partially) the ergodic assumption, type #1 partially ignore regional  
101 variability of the median response while accounting for spatial correlation in the residuals;  
102 conversely type #2 accounts for regional variabilities of the median response while neglecting the  
103 possible correlation in its residuals.

104 In this paper, we propose a novel methodology to calibrate an empirical GMM of type #2, in which  
105 some coefficients of the model vary smoothly with geographical location, adopting an approach  
106 similar to that proposed by Landwehr et al. (2016). The method we apply is the Multi-Source  
107 Mixed Geographically Weighted Regression (MS-GWR), developed *ad-hoc* by Caramenti et al.  
108 (2020) for the Italian context. MS-GWR provides a methodological framework allowing one to  
109 effectively estimate and perform inference (testing, model selection) on a regression model  
110 characterized by spatially varying coefficients – the variability being induced by multiple sources  
111 of non-stationarity (site- and event- effects in the case of GMMs). Unlike the modeling approach  
112 of Landwehr et al (2016), MS-GWR does not require any strong distributional assumption on the  
113 model' residuals (e.g., Gaussianity), either for estimation or testing. The model is developed for  
114 shallow crustal events in Italy, employing the same dataset used by Lanzano et al. (2019) to  
115 calibrate a partially non-ergodic model (namely ITA18) with fixed coefficients (*i.e.*, spatial-  
116 stationarity).

117 In the following, the MS-GWR method and the GMM calibration are outlined, then some tests and  
118 application examples are reported to show performance and application potential of the proposed  
119 approach.

120

## 121 **2. Dataset and functional form**

122

123 The calibration dataset is the same originally derived by Lanzano et al. (2019) to calibrate the  
124 ground motion model ITA18 for shallow crustal earthquakes in Italy. Differently from the original  
125 dataset, we select only the data from Italy and neighboring countries (France, Swiss and  
126 Slovenia). This because the few data (14%) selected from other regions (Japan, California,  
127 Turkey, Greece, etc.), used by Lanzano et al. (2019) to extend the maximum magnitude of model  
128 validity, cannot be used for the application of the MS-GWR method in Italy. In total, the dataset is  
129 composed by 4,784 observations of 137 events from 925 stations, recorded between 1976 and  
130 2016, with magnitudes ranging from 3.5 to 6.9. Additional details on the dataset selection are  
131 provided in Lanzano et al. (2019).

132 Figure 1a shows the source-to-station paths of the observations used for model calibration,  
133 pointing out that some areas are not well-sampled due to their lower seismicity, such as the

134 western Lombardy, the eastern Piedmont, the Trentino and southern Tyrol region, the coastal  
 135 area of Tuscany, the Salento peninsula and the south-western area of the Sicily. The magnitude–  
 136 distance distribution is shown in Figure 1b: the number of near-source records with distances  
 137 lower than 10 km is about 300, which is still relevant w.r.t. ITA18 original dataset.

138 The functional form presented by Lanzano et al. (2019) for ITA18 is:

139

$$\begin{aligned}
 140 \quad \log_{10}Y &= a + b_1(M_w - M_h)\mathbb{I}(M_w \leq M_h) + b_2(M_w - M_h)\mathbb{I}(M_w > M_h) + [c_1(M_w - M_{ref}) + \\
 141 \quad c_2] \log_{10} \sqrt{R_{JB}^2 + h^2} + c_3 \sqrt{R_{JB}^2 + h^2} + k \left[ \log_{10} \left( \frac{V_{S,30}}{800} \right) \mathbb{I}(V_{S,30} \leq 1500) + \log_{10} \left( \frac{1500}{800} \right) \mathbb{I}(V_{S,30} > \right. \\
 142 \quad \left. 1500) \right] + f_{SS}SoF_{SS} + f_{TF}SoF_{TF} + \varepsilon \qquad \qquad \qquad [1]
 \end{aligned}$$

143

144 where, Y is the observed IM (Intensity Measures), *i.e.*, the peak ground acceleration and velocity  
 145 (PGA and PGV) and 36 ordinates of acceleration response spectra at 5% damping (SA) in the  
 146 period (T) range 0.01–10s. The prediction is valid for RotD50, which is the median of the  
 147 distribution of the IMs, obtained from the combination of the two horizontal components across all  
 148 non-redundant azimuths (Boore, 2010). The explanatory variables are the moment magnitude  
 149 ( $M_w$ ), the Joyner and Boore source-to-site distance ( $R_{JB}$ ), the average seismic shear-wave  
 150 velocity from the surface to 30 m ( $V_{S,30}$ ) and the styles of faulting (SoF) which are dummy  
 151 variables, introduced to specify strike-slip (SS) and reverse fault (TF), while for normal fault types  
 152 (NF), the coefficient is zero ( $f_{NF}=0$ ). The term  $\varepsilon$  is the remaining residual, *i.e.*, the logarithmic  
 153 difference between observations and predictions.

154 In this analysis, we modify the original functional form in Eq. [1], by introducing some spatially  
 155 varying coefficients:

156

$$\begin{aligned}
 157 \quad \log_{10}Y &= a + b_1(M_w - M_h)\mathbb{I}(M_w \leq M_h) + b_2(M_w - M_h)\mathbb{I}(M_w > M_h) + [c_1(M_w - M_{ref}) + \\
 158 \quad c_2(t_e)] \log_{10} \sqrt{R_{JB}^2 + h^2} + c_3(t_e) \sqrt{R_{JB}^2 + h^2} + k(t_s) \left[ \log_{10} \left( \frac{V_{S,30}}{800} \right) \mathbb{I}(V_{S,30} \leq 1500) + \right. \\
 159 \quad \left. \log_{10} \left( \frac{1500}{800} \right) \mathbb{I}(V_{S,30} > 1500) \right] + f_1SoF_1 + f_2SoF_2 + \varepsilon \qquad \qquad \qquad [2]
 \end{aligned}$$

160

161 where the ground-motion model is calibrated for the same IMs as in Lanzano et al. (2019). The  
 162 coefficients for geometric spreading  $c_2$  and anelastic attenuation  $c_3$  are assumed dependent on  
 163 the coordinates of the event  $t_e$ ; the coefficient k of the linear scaling with  $V_{S,30}$  is instead function  
 164 of station coordinates,  $t_s$ . In the calibration of the MS-GWR model, we decide to model the spatial

165 dependencies in the same way as done by Landwehr et al. (2016), so as not to overly modify the  
 166 original functional form of ITA18. As a matter of fact, a better modeling of path effects through the  
 167 coefficients  $c_2$  and  $c_3$  should include a dependence on both event and site coordinates. However,  
 168 calibration of a local model depending on the four-dimensional vector of coordinates  $(t_e, t_s)$  would  
 169 be hardly doable in practice, because this would require calibrating the model for all the local  
 170 neighborhoods of  $(t_e, t_s)$  – *i.e.*, it would require a reasonably high amount of data around any  
 171 combination of event- and site- coordinates (*i.e.*, curse of dimensionality).

172 Differently from the study of Landwehr et al. (2016), the offset is not modeled by introducing the  
 173 spatial dependence on event and station locations, because MS-GWR was shown to be  
 174 ineffective in assessing spatially varying offset (Caramenti et al., 2020). This issue may indirectly  
 175 be solved through a random effect modeling (similarly as done in ITA18); however, regionalized  
 176 regression models based on MS-GWR are yet to be developed and this will thus be the scope of  
 177 future work.

178 In the next Section 3, we describe the general model and the estimation method used to calibrate  
 179 model [2].

180

### 181 **3. Method**

182

183 The method we consider to calibrate model in Eq. [2] lies in the framework of Geographically  
 184 Weighted Regression (GWR, Brunson et al., 1998), which extends the theory of multiple linear  
 185 regression to the case where the model coefficients are spatially varying. Denoting by  $z_i$  the  $i$ -th  
 186 observation of the response variable (the logarithm of the IM being considered when Eq. [2] is  
 187 concerned) and by  $x_{ij}$ ,  $i = 1, 2, \dots$ , the set of regressors relative to the  $i$ -th observation, the general  
 188 model we aim to estimate is:

189

$$190 \quad Z_i = \sum_{j \in C} \beta_{jC} x_{ij} + \sum_{j \in E} \beta_{jE}(t_{e,i}) x_{ij} + \sum_{j \in S} \beta_{jS}(t_{s,i}) x_{ij} + \epsilon_i \quad [3]$$

191

192 where  $\epsilon_i$  is a zero-mean random error (not necessarily Gaussian) with variance  $\sigma^2$ ,  $t_{e,i} =$   
 193  $(u_{ei}, v_{ei})$ ,  $t_{s,i} = (u_{si}, v_{si})$  denote the event- and site- coordinates, respectively, associated with the  
 194  $i$ -th observation, while  $C, E$  and  $S$  denote the set of regressors associated with the stationary  
 195 coefficients ( $C$ ), and the non-stationary coefficients ( $E$  and  $S$ ), depending on event-coordinates  
 196 ( $E$ ) or site-coordinates ( $S$ ). The difference between the model in Eq. [3] and that estimated by a  
 197 standard GWR (Fotheringham et al., 2002) is twofold: (1) a set of coefficients ( $\beta_{jC}$ ) is allowed to

198 be spatially stationary, and (2) two different sources of spatial non-stationarity are allowed – *i.e.*,  
 199 those induced by the spatial indexes  $t_e$  and  $t_s$  characterizing the sets  $E$  and  $S$  of regressors. The  
 200 key differences between the model in Eq. [3] and that of Landwehr et al (2016) rely in (1) the  
 201 parametric (Gaussian) assumptions made by these authors on the term  $\epsilon_i$ , which is here avoided,  
 202 and (2) on the nature of the coefficients  $\beta'$ s. The latter are here assumed deterministic (and  
 203 unknown), whereas they are modeled as Gaussian processes governed by coefficient-specific  
 204 covariance kernels in Landwehr et al (2016) (consistent with the Bayesian approach there  
 205 considered).

206 Following Caramenti et al (2020), to estimate the response  $Z_0$  from MS-GWR model, for a target  
 207 combination of event and site coordinates  $t_{e0} = (u_{e0}, v_{e0})$ ,  $t_{s0} = (u_{s0}, v_{s0})$  (hereafter named target  
 208 location), and regressors  $x_{0j}$ , we rely on two spatial kernels,  $K_E$  and  $K_S$ , whose role is to localize  
 209 the estimation of the model in a neighborhood of the target location, by down-weighting the  
 210 contribution of the data observed at locations far apart from the target (resp. in terms of event- or  
 211 site-coordinates). In this work, we consider as  $K_E$  and  $K_S$  two Gaussian kernels, with bandwidth  
 212 set via generalized cross-validation (GCV). Any other kernel function could be used instead, with  
 213 a potential impact on the degree of smoothness of the resulting estimates (the smoother the  
 214 kernel, the smoother the estimates). It is worth noting that the kernels  $K_E$  and  $K_S$  do not represent  
 215 coefficient-specific *covariance kernels* (used, *e.g.*, in Landwehr et al. 2016), but they rather  
 216 determine the degree of locality of the regression model in Eq. [3]. Hereafter, when referring to  
 217 the regionalized nature of the model we will either use the expression *spatial variability of the*  
 218 *coefficients* or *non-stationarity*, precisely referring the non-constant nature of the  $\beta'$ s. We will avoid  
 219 the expression *spatial correlation* instead, to avoid confusion w.r.t. the model of Landwehr et al  
 220 (2016), because the coefficients are here assumed to be deterministic (although unknown).

221 From the computational standpoint, given a target location, MS-GWR is based on an iterative  
 222 procedure which estimates in cascade the three pieces of the model in Eq. [3]. First, the constant  
 223 part is fitted, obtaining an estimate  $\hat{\beta}_{jC}$  of the coefficients  $\beta_{jC}$ . From this estimate, partial residuals  
 224 are computed by difference as  $Z_i - \sum_{j \in C} \hat{\beta}_{jC} x_{ij}$ , and then used to estimate the second piece of the  
 225 model, namely the spatially non-stationary term  $\hat{\beta}_{jE}$ . This is done through GWR based on the  
 226 spatial kernel  $K_E$  – which selects the relevant data in the neighborhood of the target event location,  
 227  $t_{e0}$ . Having obtained  $\hat{\beta}_{jE}$ , this is again used to obtain updated partial residuals, which are finally  
 228 employed to estimate the second set of non-stationary coefficients. This last step is done again  
 229 through GWR, but in the neighborhood of the site locations (thus using  $K_S$ ), eventually obtaining  
 230  $\hat{\beta}_{jS}$ .

231 As we do not aim here to describe the mathematical and algorithmic details involved in the  
232 estimation of MS-GWR model, we limit to mention two key facts. First, from the algorithmic  
233 viewpoint, the cascade described above depends on the order chosen for the terms in Eq. [3].  
234 The study of Caramenti et al. (2020) shows that estimating first the offset  $a$  leads to relevant  
235 improvements in terms of estimation accuracy and prediction power, with respect to any other  
236 estimation order. No substantial difference is instead implied by different estimation orders for the  
237 non-stationary terms. In practice, the evaluation of different choices of the order of estimate, as  
238 well as of the hyperparameters of the models (i.e., the kernel bandwidths), can be done via  
239 (generalized) cross-validation (GCV). Second, from the mathematical viewpoint, the estimation  
240 procedure can be reinterpreted as a linear estimation from the data, which greatly simplifies the  
241 estimation of the uncertainty associated with the model. Indeed, one can explicitly quantify the  
242 uncertainty in the coefficient estimation, as well as the prediction variance for a target location  $t_{e0}$ ,  
243  $t_{s0}$  and vector of regressors  $x_0 = (x_{j0}, j \in C \cup E \cup S)$ .

244 The estimated variabilities associated with the regression and error terms can be used to quantify  
245 the epistemic and aleatory uncertainty in the model. Indeed, the aleatory variability is represented  
246 by the (spatially constant) variance  $\sigma^2$  of the error term  $\epsilon_i$ , whereas the epistemic uncertainty by  
247 the (spatially non-constant) variance of the estimator  $\hat{\beta}_{\cdot,0}$ . Note that the introduction of non-  
248 stationary terms in Eq. [3] allows one to move part of the aleatory variability of the model ITA18  
249 to the regression terms, leading to a decrease in the variance of the error ( $\sigma^2 < \sigma_{ITA18}^2$ ). This  
250 entails an increase in the epistemic uncertainty associated with the model coefficients, due to the  
251 increased complexity of the GMM. However, the increase in data availability and knowledge  
252 allows for a reduction of this latter uncertainty, thus enabling one to decrease the overall  
253 uncertainty in the model.

254 We finally mention that the MS-GWR framework allows for a non-parametric inference on the  
255 model coefficients (in the sense of the distribution of the error term  $\epsilon$ ), based on a permutation  
256 approach (see Caramenti et al. (2020) for details and testing of the methods). Such setting  
257 enables one to perform model selection through hypothesis testing on the stationarity of the model  
258 coefficients (marginally or jointly on set of coefficients), as well as on their statistical significance.  
259 In this work, we do not focus on this aspect, as we rely on the results obtained by Caramenti et  
260 al. (2020) for PGA, based on the same dataset here considered. These authors run extensive  
261 inferential analyses which yielded the selection of model in Eq. [2], which is here calibrated for  
262 the 36 vibration periods being considered. The use of the same model for all the vibration periods  
263 is a standard practice in seismology (Douglas and Edwards, 2016), as it greatly simplifies the  
264 overall interpretability of the calibrated GMMs. Additional analyses run for other periods anyway



265 confirmed that model selection in these cases can be consistently made as for PGA, the p-values  
266 (Wasserstein and Lazar, 2016) of the tests being similar to those obtained in Caramenti et al.  
267 (2020) (not shown).

268

#### 269 **4. Calibration results and comparison with ITA18**

##### 270 *4.1 Stationary and spatially dependent coefficients*

271 Following the approach proposed by Caramenti et. al (2020) for MS-GWR calibration, the kernel  
272 bandwidths were set to  $h_E = 25km$  and  $h_S = 75km$  for those associated with event and site  
273 coordinates, respectively, for periods up to 5s. For periods longer than 5 seconds the bandwidths  
274 were set to  $h_E = 40km$  and  $h_S = 80km$ . Although spatially adaptive kernels could we used in  
275 principle, we prefer to keep a spatially constant kernel to reduce the number of hyperparameters  
276 of the model. The estimation order was set to  $S$ ,  $E$  and  $C$ , consistent with GCV results. All the  
277 coefficients estimated for model in Eq. [2] are provided in the electronic supplements. In particular,  
278 the spatially varying coefficients are computed for an equally-spaced grid of 10km. All the  
279 coefficient tables are also available in a GitHub repository (see *Data and Resources*).

280 Figure 2 compares the stationary coefficient of MS-GWR models with the corresponding ones of  
281 ITA18 for the SA ordinates, including PGA (*i.e.*, SA at  $T=0$ ). The values obtained by calibrating  
282 the fixed coefficients of the MS-GWR method are very similar to those obtained for ITA18, over  
283 the entire range of periods, except for a slight difference between the values of the  $b_2$  coefficient  
284 for periods longer than 5s. The latter coefficient models the scaling with the magnitude for stronger  
285 earthquakes ( $M > M_h$ ); in the case of longer periods, the value of  $M_h$  is higher (about 6.3 for  $T > 5s$ ,  
286 see Lanzano et al. 2019) and the number of data available for very strong earthquakes in this  
287 analysis is smaller than ITA18, since the foreign events have been removed from the dataset.

288 Table 1 reports the comparison of the regression parameter p-Value (Wasserstein and Lazar,  
289 2016) related to ITA18 w.r.t. that obtained for the stationary coefficients of the MS-GWR. A  
290 coefficient with a low p-value (marked as  $<0.05$ ) indicates that the corresponding term is a  
291 meaningful addition to the predictive model. This is the case for coefficients  $a$ ,  $b_1$ , and  $c_1$  for both  
292 the ITA18 and MS-GWR models. On the contrary,  $f_1$  and  $f_2$  coefficients exhibit p-values larger  
293 than 0.05 for both models, confirming that this additional variable (*i.e.*, the style of faulting) has a  
294 small impact on the model predictions (Bommer et al. 2003).

295 The maps of the spatially varying coefficients of the distance scaling for two selected ordinates of  
296 the acceleration response spectra ( $T=0.1s$  and  $1s$ ) are given in Figure 3. The values of the  
297 coefficient  $c_2$  for the geometrical spreading vary in the interval -1.1 to -1.9 and in the interval -0.9

298 and -1.7 for SA T=0.1s and 1s, respectively. In both cases, the stationary coefficients derived by  
299 ITA18 are included in the interval of the spatially varying coefficients calibrated by MS-GWR.  
300 At short period, the fastest attenuation (*i.e.*, lower  $c_3$  values) is observed in the Campania region,  
301 close to the volcanic districts of Vesuvius and Phlegrean fields, while, at long periods in the  
302 northern Piedmont region. The values of the coefficient  $c_3$  for the anelastic attenuation is included  
303 in the range -0.009 to 0.003 and range -0.005 to 0.005 for the selected parameters. The ITA18  
304 stationary coefficients are still included in the interval of  $c_3$  values of MS-GWR.  
305 From a broad look at the spatial distribution of the coefficients in Figure 3,  $c_2$  and  $c_3$  maps look  
306 anti-correlated, because regions with higher  $c_2$  have lower  $c_3$  and vice-versa. This observation  
307 suggests that the coefficients for geometric spreading and apparent anelastic attenuation may  
308 have a strong trade-off, which has already been frequently observed in the calibration of stationary  
309 coefficient models (Boore et al. 2014; Campbell and Bozorgnia, 2014). In fact, the reference  
310 model ITA18 already shows a very strong anti-correlation at T=0.1s, assuming values of  
311 Pearson's correlation index  $\rho_{c_2,c_3} = -0.99$  (see Table 1 in Lanzano et al. 2019). In order to check  
312 this issue, we estimate the spatially varying  $\rho_{c_2,c_3}$  values from the MS-GWR model and plot them  
313 in Figure 4 for the two SA ordinates. The coefficients are still strongly anti-correlated and show  
314 values below -0.9 in a large portion of the Italian territory, both at 0.1s and 1s. This result shows  
315 that, although the prediction is accurate, the interpretation of the spatial trend of the geometric  
316 and anelastic attenuation coefficients on the basis of local geology could be tricky.  
317 Another issue, partially connected with the latter, is related to the positive values that the  $c_3$   
318 coefficients assume in some areas: indeed, in such a case, the application of the model to  
319 distances above the validity limit (generally 100-200km), leads to unrealistic effects, such as the  
320 enhancement of the ground motion from a certain distance onwards. At long-periods, the most  
321 practical solution is to remove the anelastic attenuation term from the functional form, as done by  
322 Landwehr et al. (2016) for T>1s and by ITA18 for periods longer than 1.4s. On the contrary, the  
323 positive values of  $c_3$  at short periods that, for example, occurs in Po river basin (northern Italy)  
324 are likely related to wave reflections at Moho interface. As reported in Lanzano et al. (2016), "this  
325 phenomenon has been already observed by Douglas et al. (2004) in central Italy and southern  
326 Iceland and by Bragato et al. (2011) in northern Italy and is explained as the enhancement of  
327 ground motion due to S-wave reflection at the Moho discontinuity (SmS phase)". In the particular  
328 case of the Po Plain, Bragato et al. (2011) and Lanzano et al. (2016) showed that the net effect  
329 is precisely an enhancement of PGA and high frequency parameters from a certain distance  
330 onwards (> 50km). Placing  $c_3=0$  is a rough simplification that ignores these phenomena. It is  
331 necessary to adopt alternative solutions to model this term, as proposed by Lanzano et al. (2016),

332 which sets a hinge distance (around 70km) and establishes a slope change in attenuation. On  
333 the other hand, the beneficial aspect of this spatial modeling is the ability to capture faster  
334 anelastic attenuation in Central Italy, which was also observed by several authors comparing  
335 predictions with observations (Scasserra et al. 2009; Luzi et al. 2017).

336 The maps of the  $k$  coefficients of the  $V_{S,30}$  scaling are instead given in Figure 5 for the same  
337 intensity measures of Figure 3. The interval of variation of the  $k$  coefficient is quite wide at all  
338 periods, but the ITA18 values are still in the range of the MS-GWR values. At short periods,  $k$   
339 assumes in several cases slightly positive values in south-eastern Sicily and northern coast of  
340 Tuscany, that unrealistically correspond to amplifications of the median prediction as  $V_{S,30}$   
341 increases (see Kamai et al. 2014 for the expected  $V_{S,30}$  scaling). This unstable behavior is  
342 sometimes observed in the GMM regression of FAS ordinates at high frequencies (Bora et al.  
343 2015) and demonstrates that  $V_{S,30}$  and site effects are poorly correlated in this range of periods.  
344 However, looking at the spatial distribution of the stations, the positive values in the coastal part  
345 of Tuscany could be caused by the fact that there are no stations in this area to constrain the  
346 scaling with  $V_{S,30}$ . In eastern Sicily, 24 recordings from 15 stations are available: the mean site  
347 amplification (called  $\delta S2S_{ref}$ ) with respect to reference site predictions ( $V_{S,30}=800\text{m/s}$ ) prediction  
348 at the spectral period  $T=0.1\text{s}$  is estimated for each station and reported in Figure 6 as a function  
349 of the  $V_{S,30}/800$ . If we draw a regression line, whose slope approximately describes the scaling  
350 with  $V_{S,30}$ , we observe that the amplification grows as  $V_{S,30}$  increases, *i.e.*,  $k$  is positive. However,  
351 this trend is caused by the scarcity of records available in this area and is particularly conditioned  
352 by the value observed by the IT.GEA station. As a matter of fact, if the latter was excluded, one  
353 could note an opposite scaling (weakly negative).

354

#### 355 *4.2 Model variability*

356

357 The efficiency of the proposed approach for ground motion modelling is evidenced by the  
358 significant decrease in total variability ( $\sigma$ ) of the MS-GWR w.r.t. ITA18 at all periods (Figure 7a),  
359 attaining an average reduction of about 10%. The trend of sigma still presents a bump at  $T=0.1\text{s}$ ,  
360 which confirms that such a large variability is due to effects not accounted by this model, *e.g.*, the  
361 limited ability of  $V_{S,30}$  in capturing the site effect variability at high-frequencies. In any case, the  
362 aleatory variability at this period drops from 0.41 to 0.34  $\log_{10}$  units. The electronic supplements  
363 (ESUPP3) report the distribution of the total residuals as a function of magnitude, distance and  
364  $V_{S,30}$  for the two control periods. The results still confirm the goodness of the calibration, since  
365 there are no remarkable biases with the predictor variables

366 In order to assess which component of the variability is more affected by the introduction of the  
367 non-stationarity in the GMM coefficients, we *a-posteriori* decompose the total residual of the MS-  
368 GWR model into the event, station, and event- and station- corrected terms and calculate the  
369 associated variabilities. As for ITA18, a random-effects approach is used to estimate the  
370 repeatable terms more robustly. Figure 7b, c and d show a comparison of the standard deviations  
371 obtained from the decomposition of the MS-GWR residuals with those provided by the ITA18  
372 reference model. It is apparent that much of the reduction in total variability relates to the event  
373 term ( $\tau$ ), which is reduced across all periods in an amount ranging between 40 and 50%. The  
374 reduction in the site-related variability ( $\phi_{S2S}$ ) is much smaller, ranging between 5 and 10%. The  
375 remaining variability ( $\phi_0$ ), on the other hand, would be completely indifferent to the proposed MS-  
376 GWR modeling. Assuming no significant trade-off between residual components, this result  
377 suggests that the introduced spatial dependencies primarily capture differences between the  
378 sources, likely due to differences in mean stress drops. The site effect is limitedly benefited by  
379 this ground motion modeling (k dependence on station coordinates). Regional differences in  
380 seismic wave propagation, not captured by the starting functional, should be contained in the  
381 residual term cleaned of repeatable event and station effects: the fact that it is not reduced  
382 suggests that much of such effects are not captured by the introduced spatial dependencies  
383 (associated to event location), thus raising the need to introduce different parameterizations of  
384 the functional form and spatial dependencies.

385 Lanzano et al. (2019) also quantified the prediction error of ITA18 by estimating the statistical  
386 uncertainty in the median predictions, calculated on the model fit and the data distribution, as in  
387 Al-Atik & Youngs (2014). In the case of MS-GWR, the prediction uncertainty is computed by  
388 leveraging on the linear form of the estimators to account for the variability of the coefficients'  
389 estimators  $\hat{\beta}_{\cdot,0}$  (see Caramenti et al., 2020, for further details). The spatial distribution of median  
390 predictions  $\hat{y}$  and the associated epistemic uncertainty SD ( $\hat{y}$ ) (also denoted as  $\sigma_{\mu}$ ), for an  
391 example scenario ( $M_w=6.0$ ,  $R_{JB}=10\text{km}$ ,  $V_{S,30}=300\text{m/s}$  and normal faults) are reported in Figure 8  
392 for the two selected intensity measures.

393 The median predictions of the SA ordinate at  $T=0.1\text{s}$  vary from 0.15g to about 1g for the  
394 considered scenario, while at  $T=1\text{s}$ , the SA values are in the range 0.05-0.3g. The associated  
395 uncertainty varies from 0 to about 0.2 log10 units, both for short and long periods, with the lowest  
396 values in the central Apennines, where sampling is dense, and the highest in central Apulia,  
397 coastal areas of Tuscany and some areas in southern Calabria and Sicily, characterized by few  
398 and sparse data.

399 Figure 8 also reports the location of two selected sites (A and B), where we further explore the  
 400 dependency of  $\sigma_\mu$  on the different explanatory variables (Figure 9). The site A (43°N, 13°E) is  
 401 located in the area with the largest density of records, corresponding to the epicentral area of the  
 402 2016-2017 central Italy seismic sequences; the site B (41°N, 17°E) belongs to an area with sparse  
 403 and sporadic seismicity in the last 40 years, after the very strong earthquake of Irpinia ( $M_w$  6.9  
 404 23/11/1980) that occurred at a distance less than 100km.

405 As expected, the variability of the MS-GWR model tends to that of ITA18 in cases where densely  
 406 sampled sites are considered (site A): in general, the uncertainty associated with the prediction  
 407 must be larger than ITA18, because, in the new functional (Eq. 2), additional explanatory variables  
 408 (the coordinates of event and station) are included, with respect to the original functional form of  
 409 ITA18. The uncertainty associated with site B is, instead, on average three times larger than  
 410 ITA18. As in ITA18, the largest variation of  $\sigma_\mu$  depends on the earthquake magnitude: in all the  
 411 cases considered,  $\sigma_\mu$  increases at magnitude greater than 7.0, where the data sampling is poorer.  
 412 Similar behavior is observed for  $V_{S,30} < 300$  m/s. Note that the range of the Joyner-Boore distance  
 413  $R_{JB}$  in Figure 9 is [0,100] km, consistent with the bandwidths  $h_E, h_S$  selected for the estimation of  
 414 the MS-GWR. These bandwidths directly reflect on the range of validity of the model itself, which  
 415 should not be used beyond the range of the training data – similarly as for unweighted models.  
 416 Finally,  $T=0.1s$  is still the period of SA at which the higher uncertainty about the prediction is  
 417 observed.

418

## 419 **5. Cross-validation and comparison with independent events**

420 In order to validate the model, we carry out a 10-fold cross-validation, splitting the dataset  
 421 completely at random (i.e., sampling without replacement the data  $(z_i, x_{ij}, j \in C \cup E \cup S)$ ,  $i =$   
 422  $1, \dots, N$ ) in 10 folds  $F_1, \dots, F_{10}$  and comparing the (in-sample) mean squared error (MSE), defined  
 423 as:

424

$$425 \quad MSE_{10-fold} = \frac{1}{10} \sum_{j=1}^{10} \frac{\sum_{i \in F_j} (z_i - \hat{z}_{-j})^2}{N_j} \quad [4]$$

426

427 where  $N_j$  is the number of data,  $z_i$  are the observations and  $\hat{z}_{-j}$  are the predicted value using the  
 428 proposed model error for 5 intensity measures - PGA, SA (0.1s), SA (0.3s), SA (1s), SA (3s) -  
 429 using all folds except for  $F_j$ . To allow for a fair comparison with ITA18, predictions of ITA18 are  
 430 calculated following the same CV procedure, by recalibrating each time the model upon the same

431 dataset considered for MS-GWR. Note that the calibration is here based on a restriction of the  
432 dataset originally considered to calibrate ITA18 (see § 2). Regression coefficients obtained for  
433 the restricted dataset where however equivalent to those originally obtained by Lanzano et al.  
434 (2019) (not shown).

435 Results (Figure 10) show that MS-GWR leads to improved results with respect to ITA18 over all  
436 the considered periods, supporting the introduction of spatially varying coefficients. The  
437 improvement of the prediction of MS-GWR model with respect to ITA18 is particularly evident at  
438 high frequencies, such as for 0.1s, for which the median value of  $MSE_{10-fold}$  and the associated  
439 standard deviation are reduced by 28% and 25%, respectively.

440 The prediction performance of the proposed model is also assessed through a spectral  
441 comparison between the predicted ground motion parameters and the observed ones at given  
442 recording sites for some independent events (*i.e.*, not included in the calibration dataset). The  
443 independent earthquakes used in this analysis are reported in Table 2. The records used for  
444 testing are taken from the ITACA database (see *Data and Resources*).

445 First, we make a qualitative comparison between some observed spectra of the earthquakes in  
446 Table 2 and the predictions of the ITA18 and MS-GWR models in Figure 11. The illustrative  
447 recordings are representative of three possible outcomes: a) the MS-GWR prediction is closer to  
448 the observation of ITA18 (top panel); b) the MS-GWR and ITA18 predictions are similar, although  
449 far from observation (bottom left); c) ITA18 predicts the observation better than MS-GWR (bottom  
450 right). Scenario (a) occurs in the majority of the cases: in particular, the two cases given as  
451 examples relate to an independent event that occurred in a densely sampled area of the  
452 calibration dataset. Scenario (b) is less frequent and generally occurs when the observation can  
453 be considered as an outlier for both predictive models. Scenario (c) is quite rare, but in any case,  
454 MS-GWR always returns fairly regular predicted spectra without bumps. More generally, in areas  
455 where few data are available, the MS-GWR model tends to make predictions very similar to that  
456 of the corresponding stationary model.

457 In order to quantify the average gain of MS-GWR compared to ITA18, Figure 12 reports the  
458 boxplot of the absolute value of the standardized residuals of the four selected seismic events for  
459 the same intensity measures of Figure 10. MS-GWR, on average, leads to either better or  
460 comparable results to ITA18 for the events of Termoli, Barletta and Muccia. Moreover, in the  
461 densely sampled areas, the residuals are characterized by a very low variability, as for the event  
462 of Muccia. No improvements are observed for the event of Siracusa, where the record sampling  
463 of the calibration dataset is still sparse and does not allow for a significant improvement in  
464 predictions and associated variabilities, compared to ITA18.

465

## 466 **6. Discussion and Conclusions**

467

468 The challenging goal of introducing the regionalization into the ground motion modelling of Italy  
469 led us to implement and test spatial regression techniques in the phase of predictive model  
470 calibration. We drew inspiration from the work of Landwehr et al. (2016) for California to develop  
471 a method that introduces spatial non-stationarity into the coefficients of the model. The method  
472 proposed here is called Multi-Source Geographically-Weighted Regression (MS-GWR) and  
473 consists of a family of local linear regression models, accounting for the variability of the  
474 parameters due to either event- or site-effects. All the statistical details of the methodology are  
475 given in Caramenti et al. (2020) where results are reported for the case of the peak ground  
476 acceleration. In this paper, we have tested this regression technique for the ground motion  
477 prediction of the shallow active crustal events in Italy and discussed its results with respect to  
478 several intensity measures of engineering interest, such as the ordinates of acceleration elastic  
479 response spectra; we also compared our main findings with those of the corresponding model  
480 with stationary coefficients, named ITA18 published by Lanzano et al. (2019). In order to carry  
481 out a homogeneous comparison between the proposed and existing models as well as to assess  
482 the improvements appropriately, we kept the functional form and the calibration dataset as  
483 invariant as possible. In addition, the spatial dependencies of the parameters have been  
484 introduced in a simplified manner, following the experience gained in the paper by Landwehr et  
485 al. (2016).

486 In this regard, Figure 13 returns the spatial distribution of the total residuals ( $y - \hat{y}$ ) of the  
487 2018/04/10  $M_w$  4.6 Muccia earthquake (see also Table 2 for additional information) using the  
488 ITA18 and the predictive model proposed in this paper using the MS-GWR. The ITA18 residuals  
489 show a spatial trend with highly marked azimuthal dependencies, highlighted by large positive  
490 residuals (i.e., predictions larger than the observations) at short-periods (Figure 13a) in the  
491 Eastern sectors, with respect to the epicenter; while the remaining residuals (prevailing in the  
492 Western sectors) are, on average, negative. At longer periods, ITA18 residuals are moderately  
493 positive almost in the whole investigated area (Figure 13c). For both spectral ordinates, the spatial  
494 trends are less marked when we apply the MS-GWR technique: at short-period (Figure 13b), the  
495 positive residuals in the North-Eastern sector reduce in absolute value, while, in the epicentral  
496 area, no spatial trend is visible at the plot scale; at longer periods, the negative bias observed on  
497 ITA18 is corrected and the residuals do not exhibit any significant pattern.

498 This simple example shows how the application of the MS-GWR method results in a significant  
499 improvement in the model predictions, which can be interpreted as a partial removal of the ergodic  
500 assumption. Nevertheless, even if the MS-GWR model is able to explain a relevant part of the  
501 spatial variability observed in the data compared to ITA18, some caveats arise with respect to the  
502 starting assumptions, when we move to spatially-variable models:

503 - The spatial dependence for the geometric spreading and anelastic attenuation  
504 coefficients, based only on the event coordinates, is rather simplified. In fact, these terms  
505 depend on the source-to-site path, thus on both the event and station coordinates. For  
506 instance, to account for regional effects, some authors use a spatially-independent scaling  
507 with distance and, define anelastic attenuation correctives for homogeneous zones that  
508 are based on the site-dependent propagation properties of the media (Campbell &  
509 Bozorgnia 2014; Kotha et al. 2020); other authors use grid-based approaches to group  
510 and calculate repeatable path terms, obtained from the decomposition of residuals  
511 (Dawood and Rodriguez-Marek, 2013; Abrahamson et al. 2019; Sgobba et al. 2021). The  
512 latter approach would certainly be preferable for future developments of MS-GWR model,  
513 but it faces with a lack of data that often does not allow estimating corrections for all  
514 source-site paths;

515 - The coefficients for geometric spreading  $c_2$  and anelastic attenuation  $c_3$  are affected by a  
516 strong trade-off, showing a significant degree of anti-correlation in large part of the study  
517 area. This undesirable effect is very common in GMM calibration (Boore et al., 2014;  
518 Campbell and Bozorgnia, 2014) and the starting model (ITA18) is also affected by. This  
519 evidence implies that we cannot give physically-consistent interpretation to the observed  
520 spatial trends of the MS-GWR coefficients on the basis of the geological setting at a  
521 regional scale. In this respect, there is no unique solution as this effect is also related to  
522 the way in which spatial scaling is modeled with distance: Boore et al. (2014) suggest to  
523 perform the calibration in multiple steps to better control the trade-off; other authors (e.g.  
524 Campbell & Bozorgnia, 2014) suggest to separate data for the  $c_2$  and  $c_3$  calibration by  
525 distance threshold (e.g. within 50km for geometrical spreading and >50km for anelastic  
526 attenuation);

527 - The coefficient  $c_3$  tends to assume weakly positive values in some areas, causing, as an  
528 undesired effect, an increase of the seismic motion with distance increasing, generally  
529 beyond the limit of model validity. At long-periods, this coefficient can be set to zero since  
530 the contribution of anelastic attenuation is negligible; at short-periods, instead, this  
531 instability can be related to physical phenomena that can alter the expected attenuation



532 trend with distance, as it happens in the Po Plain from a certain distance onwards due to  
533 wave reflections at the Moho discontinuity. In the latter case, setting  $c_3$  to zero means  
534 ignoring the physical phenomenon and, on the contrary, it would be more appropriate to  
535 take it into account in the modelling, as, for example, proposed by Lanzano et al. (2016);  
536 - For short-periods, the scarcity of recorded data and the lack of recording stations in some  
537 areas could cause instabilities in the calculation of scaling with  $V_{S,30}$  (coefficient  $k$ ), which  
538 could take on positive values, contrary to what is expected from physics (Kamai et al.  
539 2014). Until additional records are available, a practical solution to control this instability  
540 may be to correct *a-posteriori* the  $k$  coefficient, by setting to zero when it assumes positive  
541 values. Another solution could be to increase the kernel bandwidth  $h_s$ , in order to enlarge  
542 the sampling, but this would then make the prediction of motion less "local";  
543 - The model proposed in this study, unlike Landwehr et al. (2016), does not introduce spatial  
544 dependencies of the offset on the geographical coordinates of the recording site or event;  
545 this modelling assumption could limit the effectiveness of the approach in fully capturing  
546 the variability of the GMM. This issue could be mitigated by extending MS-GWR to a  
547 mixed-effects framework, an approach which is commonly adopted to remove the ergodic  
548 assumption on (not-regionalized) GMM models. In this paper, we have performed *a-*  
549 *posteriori* estimate of the repeatable site and event terms, with the purpose to verify which  
550 of the components of the variability are more affected by the non-stationary modeling. As  
551 a result, the MS-GWR modelling mainly allows to describe the differences in the level of  
552 ground motion for source areas characterized by average stress drops due to different  
553 dynamic regimes, rather than capturing differences related to the properties of the media  
554 in which seismic waves propagate.

555 In conclusion, the model proposed in this article provides promising results, but the  
556 abovementioned modelling issues must be tackled to improve the predictive power of the model.  
557 The latter goal could be certainly achieved by enlarging the calibration dataset with small  
558 magnitude and broadband records and additional data from neighboring countries. This will  
559 significantly improve predictions compared to the model presented herein in areas where  
560 sampling is poor, such as Apulia and Sicily regions. In addition, the cross-correlation among  
561 different periods could be taken into account, to build a joint probabilistic model for the IMs at  
562 different periods; this would potentially allow for enhanced point predictions and joint uncertainty  
563 assessment. A geostatistical approach based on functional data analysis for spatial data (Ramsay  
564 and Silverman, 2005; Menafoglio and Secchi 2017) has been recently proposed to deal with  
565 profiles of IMs over all vibration periods (Menafoglio et al., 2020), showing promising results in

566 the generation of shaking scenarios from the corrective terms of ITA18 (see also Sgobba et al.,  
567 2019). However, more research is needed in this setting, to develop regionalized (non-stationary)  
568 functional models to be used in the formulation of non-ergodic GMMs.

569

## 570 **7. Data and resources**

571 The report by Caramenti et al. (2020) is publicly available at [https://mox.polimi.it/publication-  
572 results/?id=917&tipo=add\\_gmox](https://mox.polimi.it/publication-<br/>572 results/?id=917&tipo=add_gmox). All data used in this article came from published sources listed  
573 in the references. The accelerometric waveforms used in this study are published in the following  
574 databases: i) Engineering Strong-Motion database (ESM, <http://esm-db.eu>) and ii) ITalian  
575 ACcelerometric Archive (ITACA, <http://itaca.mi.ingv.it>). The complete list of the GMMs, published  
576 in peer-reviewed papers, is made available with a short description by John Douglas at  
577 <http://www.gmpe.org.uk>. The coefficient tables of the MS-GWR calibration presented here are  
578 also available in a GitHub repository at <https://github.com/lucaramenti/ms-gwr> . All the sources  
579 are last accessed in January 2021.

580 The electronic supplements of this paper include: i) a table with the stationary coefficients  
581 obtained from MS-GWR regression (TableS1.csv); ii) a table with the spatially varying coefficient  
582  $c_2$  for a 10km equally-spaced grid (TableS2.csv); iii) a table with the spatially varying coefficient  
583  $c_3$  for a 10km equally-spaced grid (TableS3.csv); iv) a table with the spatially varying coefficient  $k$   
584 for a 10km equally-spaced grid (TableS4.csv); v) a pdf file with the plot of the total residuals of  
585 MS-GWR model against different explanatory variables (FigureS5.pdf).

586

## 587 **8. Acknowledgments**

588 This study is partially funded by INGV-DPC agreement B1 2019-2021, with the aim of promoting  
589 research activities in the field of seismic hazard in Italy. Francesca Pacor and Lucia Luzi are  
590 acknowledged for their support in this research and for the coordination of the activities for the  
591 accelerometric databases developments and ground motion modelling. We would also like to  
592 thank Sreeram Reddy Kotha and another anonymous reviewer of the paper for their valuable  
593 comments, that helped us in the revision phase of the manuscript.

594

595 **Reference**

596

597 Abrahamson, N. A., W. J Silva, and R. Kamai (2014). Summary of the ASK14 ground motion  
598 relation for active crustal regions, *Earthquake Spectra* 30(3) 1025-1055.

599 Abrahamson, N.A., Kuehn, N.M., Walling, M. and Landwehr, N., 2019. Probabilistic Seismic  
600 Hazard Analysis in California Using Nonergodic Ground-Motion Models. *Bull. Seismol. Soc. Am.*  
601 109(4):1235-1249.

602 Akkar, S., Sandikkaya, M.A. and Bommer, J.J., 2014. Empirical ground-motion models for  
603 point-and extended-source crustal earthquake scenarios in Europe and the Middle East. *Bull.*  
604 *Earthq. Eng.* 12(1):359-387.

605 Al Atik, L., N. Abrahamson, J. J. Bommer, F. Scherbaum, F. Cotton, and N. Kuehn (2010).  
606 The variability of ground-motion prediction models and its components. *Seismol. Res. Lett.* 81(5)  
607 794-801.

608 Al Atik, L. and R.R. Youngs (2014). Epistemic uncertainty for NGA-West2 models.  
609 *Earthquake Spectra* 30(3) 1301-1318.

610 Anderson, J. G., and J. N. Brune (1999). Probability seismic hazard analysis without the  
611 ergodic assumption, *Seismol. Res. Lett.* 70,19–28.

612 Anderson, J. G. and Y. Uchiyama (2011). A Methodology to Improve Ground-Motion  
613 Prediction Equations by Including Path Corrections, *Bull. Seismol. Soc. Am.* 101(4), 1822–1846.

614 Bazzurro, P., and C. A. Cornell (2004). Nonlinear soil-site effects in probabilistic seismic-  
615 hazard analysis, *Bull. Seismol. Soc. Am.* 94, 2110–2123.

616 Bindi, D., M. Massa, L. Luzi, G. Ameri, F. Pacor, R. Puglia, and P. Augliera (2014). Pan-  
617 European ground-motion prediction equations for the average horizontal component of PGA,  
618 PGV, and 5%-damped PSA at spectral periods up to 3.0 s using the RESORCE dataset. *Bull.*  
619 *Earthq. Eng.* 12(1) 391-430.

620 Bommer, J. J., J. Douglas, and F. O. Strasser (2003). Style-of-faulting in ground-motion  
621 prediction equations, *Bull. Earthq. Eng.* 1, 171–203.

622 Boore, D. M., J. P. Stewart, E. Seyhan, and G. Atkinson (2014). NGA-West2 equations for  
623 predicting PGA, PGV, and 5% damped PSA for shallow crustal earthquakes. *Earthquake Spectra*,  
624 30(3) 1057-1085.

625 Boore, D.M., 2010. Orientation-independent, nongeometric-mean measures of seismic  
626 intensity from two horizontal components of motion. *Bull. Seismol. Soc. Am.* 100(4) 1830-1835.

627 Boore, D. M., and J. J. Bommer (2005). Processing of strong-motion accelerograms: Needs,  
628 options and consequences, *Soil Dynam. Earthq. Eng.* 25, 93–115.

629 Bora, S.S., F. Scherbaum, N. Kuehn, P. Stafford, and B. Edwards (2015). Development of  
630 a response spectral ground-motion prediction equation (GMPE) for seismic-hazard analysis from  
631 empirical Fourier spectral and duration models. *Bull. Seismol. Soc. Am.* 105(4) 2192-2218.

632 Bozorgnia, Y. et al. (2014). NGA-West2 research project. *Earthquake Spectra*, 30(3) 973-  
633 987.

634 Bragato, P. L., M. Sukan, P. Augliera, M. Massa, A. Vuan, and A. Sarao (2011). Moho  
635 reflection effects in the Po Plain (northern Italy) observed from instrumental and intensity data,  
636 *Bull. Seismol. Soc. Am.* 10(5) 2142–2152.

637 Brunson, C., A. S. Fotheringham, and M. Charlton (1998). Geographically Weighted  
638 Regression - Modelling spatial non-stationarity, *J. Royal Statistical Society: Series D (The*  
639 *Statistician)* 47(3) 431-443.

640 Campbell, K.W., and Y. Bozorgnia (2014). NGA-West2 ground motion model for the  
641 average horizontal components of PGA, PGV, and 5% damped linear acceleration response  
642 spectra, *Earthquake Spectra* 30(3) 1087-1115.

643 Caramenti, L., A. Menafoglio, S. Sgobba, and G. Lanzano (2020). Multi-source mixed  
644 geographically weighted regression for seismic ground motion modelling. MOX-report 67/2020,  
645 Politecnico di Milano. [https://mox.polimi.it/publication-results/?id=917&tipo=add\\_qmox](https://mox.polimi.it/publication-results/?id=917&tipo=add_qmox)

646 Cauzzi, C., E. Faccioli, M. Vanini, and A. Bianchini (2015). Updated predictive equations for  
647 broadband (0.01–10 s) horizontal response spectra and peak ground motions, based on a global  
648 dataset of digital acceleration records. *Bull. Earthq. Eng.* 13(6) 1587-1612.

649 Chao, S.H., C.M. Lin, C.H. Kuo, J.Y. Huang, K.L. Wen, and Y.H. Chen (2020). Implementing  
650 horizontal-to-vertical Fourier spectral ratios and spatial correlation in a ground-motion prediction  
651 equation to predict site effects. *Earthquake Spectra*, in press.

652 Chiou, B. S. J., and R. R. Youngs (2014). Update of the Chiou and Youngs NGA model for  
653 the average horizontal component of peak ground motion and response spectra. *Earthquake*  
654 *Spectra*, 30(3), 1117-1153.

655 Cramer, C. H. (2003). Site seismic-hazard analysis that is completely probabilistic, *Bull.*  
656 *Seismol. Soc. Am.* 93(4) 1841–1846.

657 Dawood H. M., and A. Rodriguez-Marek (2013). A Method for Including Path Effects in  
658 Ground-Motion Prediction Equations: An Example Using the Mw 9.0 Tohoku Earthquake  
659 Aftershocks, *Bull. Seismol. Soc. Am.* 103(2B):1360–1372.

660 Douglas, J., P. Suhadolc, and G. Costa (2004). On the incorporation of the effect of crustal  
661 structure into empirical strong ground motion estimation, *Bull. Earthq. Eng.* 2, 75–99.

662 Douglas, J., and B. Edwards (2016). Recent and future developments in earthquake ground  
663 motion estimation. *Earth-Science Reviews* 160 203-219.

664 Esposito, S., and I. Iervolino (2012). Spatial correlation of spectral acceleration in European  
665 data, *Bull. Seismol. Soc. Am.* 102, 2781–2788.

666 Fotheringham, S., C. Brunsdon, and M. Charlton (2002). *Geographically Weighted*  
667 *Regression - the analysis of spatially varying relationships*. John Wiley & Sons Ltd.

668 Goda, K, Atkinson, GM (2010) Intraevent spatial correlation of ground-motion parameters  
669 using SK-net data. *Bulletin of the Seismological Society of America* 100: 3055–3067.

670 Kamai, R., N.A. Abrahamson, and W.J. Silva (2014). Nonlinear horizontal site amplification  
671 for constraining the NGA-West2 GMPEs, *Earthquake Spectra* 30(3) 1223-1240.

672 Kotha, S. R., D. Bindi, and F. Cotton (2016). Partially non-ergodic region specific GMPE for  
673 Europe and Middle-East. *Bull. Earthq. Eng.* 14(4) 1245-1263.

674 Kotha, S. R., G. Weatherill, D. Bindi, and F. Cotton (2020). A regionally-adaptable  
675 ground-motion model for shallow crustal earthquakes in Europe. *Bull. Earthq. Eng.* 18 4091–4125.

676 Kuehn, N. M., and N. Abrahamson (2020). Spatial correlations of ground motion for non-  
677 ergodic seismic hazard analysis, *Earthq. Eng. Struct. Dyn.* 49 4–23.

678 Landwehr, N., N. M. Kuehn, T. Scheffer, and N. Abrahamson (2016). A nonergodic ground-  
679 motion model for California with spatially varying coefficients. *Bull. Seismol. Soc. Am.* 106(6)  
680 2574-2583.

681 Lanzano G., L. Luzi, F. Pacor, C. Felicetta, R. Puglia, S. Sgobba, and M. D'Amico (2019).  
682 A revised ground motion prediction model for shallow crustal earthquakes in Italy, *Bull. Seismol.*  
683 *Soc. Am.* 109(2) 525-540.

684 Lanzano, G., F. Pacor, L. Luzi, M. D'Amico, R. Puglia, and C. Felicetta (2017). Systematic  
685 source, path and site effects on ground motion variability: The case study of Northern Italy, *Bull.*  
686 *Earthq. Eng.* 15(11) 4563–4583.

687 Lanzano, G., M. D'Amico, C. Felicetta, R. Puglia, L. Luzi, F. Pacor, and D. Bindi (2016).  
688 Ground-motion prediction equations for region-specific probabilistic seismic-hazard analysis. *Bull.*  
689 *Seismol. Soc. Am.* 106(1) 73-92.

690 Lin, P.-S., B. Chiou, N. Abrahamson, M. Walling, C.-T. Lee, C.-T. Cheng (2011) Repeatable  
691 source, site, and path effects on standard deviation for empirical ground-motion prediction  
692 models. *Bull. Seismol. Soc. Am.* 101(5) 2281–2295.

693 Luzi, L., D. Bindi, R. Puglia, F. Pacor, and A. Oth (2014). Single-station sigma for Italian  
694 strong-motion stations. *Bull. Seismol. Soc. Am.* 104(1) 467–483.

695 Luzi, L., F. Pacor, R. Puglia, G. Lanzano, C. Felicetta, M. D’Amico, A. Michelini, L. Faenza,  
696 V. Lauciani, I. Iervolino, and G. Baltzopoulos (2017). The central Italy seismic sequence between  
697 August and December 2016: Analysis of strong-motion observations, *Seismol. Res. Lett.* 88(5)  
698 1219-1231.

699 Menafoglio, A., and P. Secchi (2017) Statistical analysis of complex and spatially dependent  
700 data: a review of object-oriented spatial statistics, *Eur J Oper Res* 258(2) 401–410.

701 Menafoglio, A., S. Sgobba, G. Lanzano, and F. Pacor (2020) Simulation of seismic ground  
702 motion fields via object-oriented spatial statistics with an application in Northern Italy, *Stoch.*  
703 *Environm. Res. Risk Assess.* 32(12) 3421-3437.

704 Park, J., P. Bazzurro, and J. W. Baker (2007). Modeling spatial correlation of ground motion  
705 intensity measures for regional seismic hazard and portfolio loss estimation, *Appl. Stat. Prob. Civ.*  
706 *Eng.* 1–8.

707 Ramsay, J, and B. Silverman (2005) *Functional data analysis*, 2nd edn. Springer, New York.

708 Rodriguez-Marek, A., G. A. Montalva, F. Cotton, and F. Bonilla (2011). Analysis of single-  
709 station standard deviation using the KiK-net data. *Bull. Seismol. Soc. Am.* 101(3) 1242–1258.

710 Sabetta, F., and A. Pugliese (1987). Attenuation of peak horizontal acceleration and velocity  
711 from Italian strong-motion records, *Bull. Seismol. Soc. Am.* 77(5) 1491-1513.

712 Sabetta, F., and A. Pugliese (1996). Estimation of response spectra and simulation of  
713 nonstationary earthquake ground motions, *Bull. Seismol. Soc. Am.* 86(2) 337-352.

714 Sahakian, V.J., A. Baltay, T.C. Hanks, J. Buehler, F.L. Vernon, D. Kilb, and N.A.  
715 Abrahamson (2019). Ground motion residuals, path effects, and crustal properties: A pilot study  
716 in Southern California, *J. Geophys. Res. Solid Earth*, 124(6):5738-5753.

717 Scasserra, G., J. P. Stewart, P. Bazzurro, G. Lanzo, and F. Mollaioli (2009). A comparison  
718 of NGA ground-motion prediction equations to Italian data, *Bull. Seismol. Soc. Am.* 99, no. 5,  
719 2961–2978.

720 Schiappapietra, E., and J. Douglas (2020). Modelling the spatial correlation of earthquake  
721 ground motion: insights from the literature, data from the 2016-2017 central Italy earthquake  
722 sequence and ground-motion simulations, *Earth- Science Reviews* 203.

723 Sgobba, S., G. Lanzano, F. Pacor, R. Puglia, M. D’Amico, C. Felicetta, and L. Luzi (2019).  
724 Spatial correlation models of systematic site and path effects for Ground-Motion fields in Northern  
725 Italy, *Bull. Seismol. Soc. Am.* 109(4) 1419–1434.

726 Sgobba S., L. Lanzano, and F. Pacor (2021). Empirical non-ergodic shaking scenarios  
727 based on spatial correlation models: an application to central Italy. *Earthq. Eng. Struct. Dyn.* 50  
728 60-80.

729 Sokolov, V, Wenzel, F (2011) Influence of spatial correlation of strong ground motion on  
730 uncertainty in earthquake loss estimation. *Earthquake Engineering and Structural Dynamics* 40:  
731 993–1009.

732 Stafford, P. J. (2014). Crossed and nested mixed-effects approaches for enhanced model  
733 development and removal of the ergodic assumption in empirical ground-motion models, *Bull.*  
734 *Seismol. Soc. Am.* 104(2) 702-719.

735 Stucchi, M., C. Meletti, V. Montaldo, H. Crowley, G. M. Calvi, and E. Boschi (2011). Seismic  
736 hazard assessment (2003–2009) for the Italian building code, *Bull. Seismol. Soc. Am.* 101(4)  
737 1885-1911.

738 Villani, M., and N. A. Abrahamson (2015) Repeatable site and path effects on the ground-  
739 motion sigma based on empirical data from Southern California and simulated waveforms from  
740 the CyberShake platform, *Bull. Seismol. Soc. Am.* 105(5) 2681–2695.

741 Wasserstein, R. L., and N. A. Lazar (2016). The ASA’s statement on p-values: Context,  
742 process, and purpose, *Am. Stat.* 70, no. 2, 129–133.

743            Woessner, J. et al. (2015). The 2013 European seismic hazard model: key components and  
744 results, Bull. Earthq. Eng. 13(12) 3553-3596.

745 **Full mailing address of each author**

746

747 1. **Giovanni Lanzano**, Istituto Nazionale di Geofisica e Vulcanologia, Via Alfonso  
748 Corti 12, 20133 Milano, Italy, giovanni.lanzano@ingv.it;

749 2. **Sara Sgobba**, Istituto Nazionale di Geofisica e Vulcanologia, Via Alfonso Corti 12,  
750 20133 Milano, Italy, sara.sgobba@ingv.it;

751 3. **Luca Caramenti**, MOX, Department of Mathematics, Politecnico di Milano, Via  
752 Bonardi 9, Milano, Italy, luca.caramenti@mail.polimi.it;

753 4. **Alessandra Menafoglio**, MOX, Department of Mathematics, Politecnico di  
754 Milano, Via Bonardi 9, Milano, Italy, alessandra.menafoglio@polimi.it

755

756 **Tables**

757

758 **Table 1.** P-Values obtained from the model regression.

<b>Coefficients</b>	<b>SA-T=0.1s</b>		<b>SA-T=1s</b>	
	<b>ITA18</b>	<b>MS-GWR</b>	<b>ITA18</b>	<b>MS-GWR</b>
<i>a</i>	<< 0.05	<< 0.05	<< 0.05	<< 0.05
<i>b</i> <sub>1</sub>	< 0.05	<< 0.05	<< 0.05	<< 0.05
<i>b</i> <sub>2</sub>	0.137	0.133	< 0.05	0.149
<i>c</i> <sub>1</sub>	<< 0.05	<< 0.05	<< 0.05	<< 0.05
<i>f</i> <sub>1</sub>	< 0.05	< 0.05	0.586	< 0.05
<i>f</i> <sub>2</sub>	0.526	0.118	0.935	0.103

759

760



761 **Table 2.** List of independent events for model validation. In italics the ITACA event ID.

<b>Municipality name <i>ITACA event ID</i></b>	<b>Event Date</b>	<b>Moment magnitude (Mw)</b>	<b>Epicenter latitude [°]</b>	<b>Epicenter longitude [°]</b>	<b>Number of records</b>
Muccia, MC <i>EMSC-20180410_0000011</i>	2018-04-10 03:11:31	4.6	43.0687	13.03650	174
Termoli, CB <i>EMSC-20180816_0000090</i>	2018-08-16 18:19:06	5.1	41.87420	14.86480	167
Barletta, BT <i>EMSC-20190521_0000022</i>	2019-05-21 08:13:32	4.0	41.29920	16.30030	51
Siracusa, SR <i>IT-1990-0003</i>	1990-12-13 00:24:26	5.6	37.19500	15.46800	7

762

763

764 **List of figure captions**

765

766 **Figure 1.** Calibration dataset: a) location of earthquake events and recording stations; b)  
767 moment magnitude  $M_w$  vs Joyner-Boore distance scatter plot.

768 **Figure 2.** Stationary coefficients of ITA18 vs ITA18\_MS-GWR: a) offset  $a$ ; b) magnitude  
769 scaling coefficient  $b_1$ ; c) magnitude scaling coefficient  $b_2$ ; d) strike-slip coefficient  $f_1$ ; e)  
770 thrust fault coefficient  $f_2$ ; f) magnitude-dependent geometrical spreading coefficient  $c_1$ .

771 **Figure 3.** Maps of the spatially variable coefficients for the distance scaling: a)  
772 geometrical spreading coefficient  $c_2$  for SA-T=0.1s; b) geometrical spreading coefficient  
773  $c_2$  for SA-T=1s; c) anelastic attenuation coefficient  $c_3$  for SA-T=0.1s; d) anelastic  
774 attenuation coefficient  $c_3$  for SA-T=1s. The values of stationary coefficients obtained by  
775 ITA18 calibration are given in the plot.

776 **Figure 4.** Maps of the Pearson correlation index between  $c_2$  and  $c_3$  coefficients ( $\rho_{c_2,c_3}$ ): a)  
777 SA T=0.1s; b) SA T=1s.

778 **Figure 5.** Maps of the spatially variable coefficients for  $V_{S,30}$  scaling coefficient  $k$  at: a)  
779 SA-T=0.1s; b) SA-T=1s. The values of stationary coefficients obtained by ITA18  
780 calibration are given in the plot.

781 **Figure 6.** Mean site amplification ( $\delta S_2 S_{ref}$ ) with respect to ITA18 predictions at  
782  $V_{S,30}=800\text{m/s}$  as a function of  $V_{S,30}/800$  for selected station in south-eastern Sicily.

783 **Figure 7.** Standard deviation components vs. period: a) total ( $\sigma$ ); b) between-event ( $\tau$ ); c)  
784 site-to-site ( $\phi_{S_2S}$ ); d) event- and site- corrected residuals ( $\phi_0$ ).

785 **Figure 8.** Maps of the median predictions  $\hat{y}$  and associated epistemic uncertainty  $SD(\hat{y})$   
786 for the scenario  $M_w=6.0$ ,  $R_{JB}=10\text{km}$ ,  $V_{S,30}=300\text{m/s}$  and normal faults: a)  $\hat{y}$  of  $\log_{10}SA$  at  
787  $T=0.1\text{s}$ ; b)  $SD(\hat{y})$  of  $\log_{10}SA$  at  $T=0.1\text{s}$ ; c)  $\hat{y}$  of  $\log_{10}SA$  at  $T=1\text{s}$ ; d)  $SD(\hat{y})$  of  $\log_{10}SA$  at  
788  $T=1\text{s}$ .

789 **Figure 9.** Epistemic uncertainty of MS-GWR model and ITA18 as a function of the  
790 predictive variables for the sites A and B in Figure 6: a) period; b) moment magnitude  $M_w$ ;  
791 c) Joyner-Boore distance  $R_{JB}$ ; d)  $V_{S,30}$ .

792 **Figure 10.** Boxplot of MSE by 10-fold cross validation at several periods: comparison  
793 between ITA18 model (light-colored error bars) and MS-GWR model (dark-colored error  
794 bars).

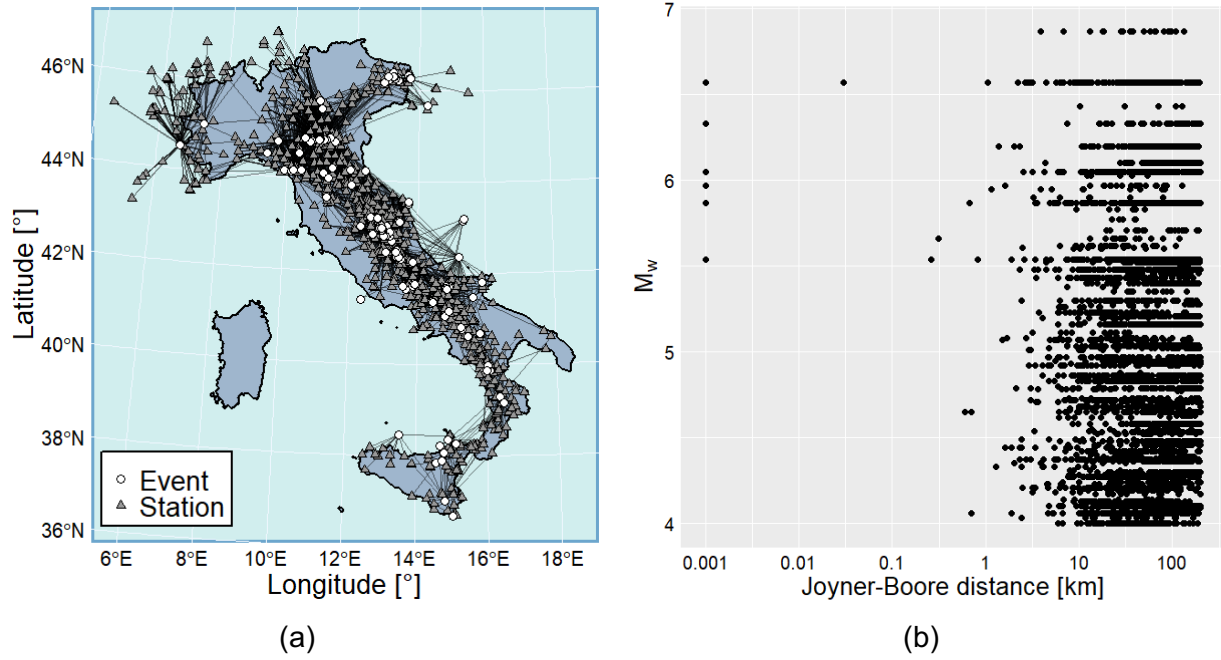
795 **Figure 11.** Observed vs predicted spectra.

796 **Figure 12.** Boxplot of the standardized residuals for the selected independent events of  
797 Table 1:  $M_w$  4.6 2018/04/10 Muccia (a),  $M_w$  5.1 2018/08/16 Termoli (b),  $M_w$  4.0  
798 2019/05/21 Barletta (c) and  $M_w$  5.6 1990/12/13 Siracusa (d). The predictions by ITA18  
799 model (light-colored error bars) and MS-GWR model (dark-colored error bars) are  
800 compared.

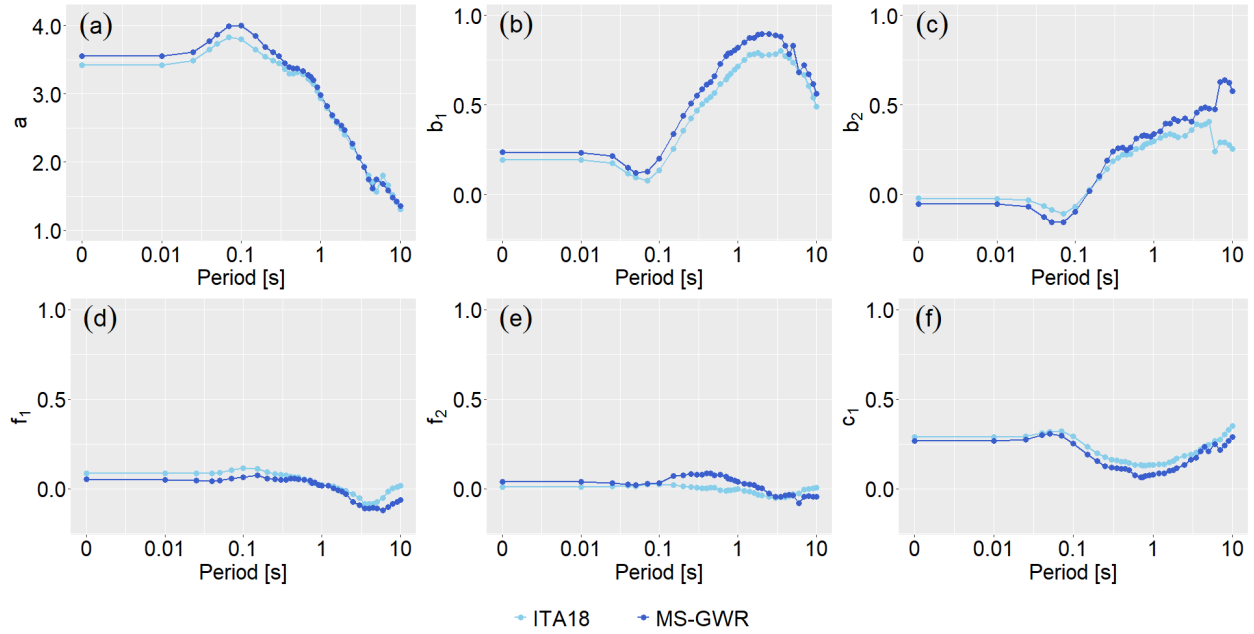
801 **Figure 13.** Total residuals of the 2018/04/10  $M_w$  4.6 Muccia earthquake: a) ITA18, SA-  
802 T=0.1s; b) MS-GWR, SA-T=0.1s; c) ITA18, SA-T=1s; b) MS-GWR, SA-T=1s.

803

804

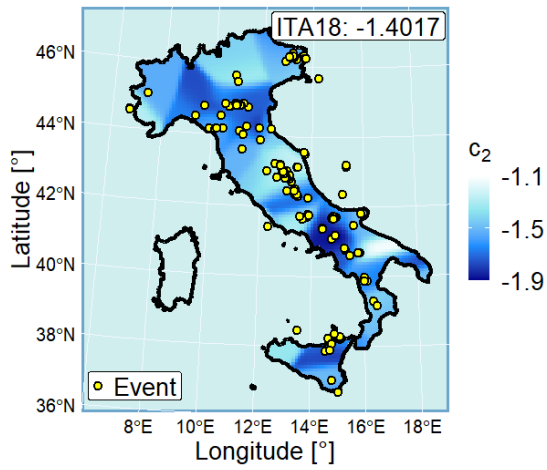


805 **Figure 1.** Calibration dataset: a) location of earthquake events and recording stations; b) moment  
806 magnitude  $M_w$  vs Joyner-Boore distance scatter plot.  
807

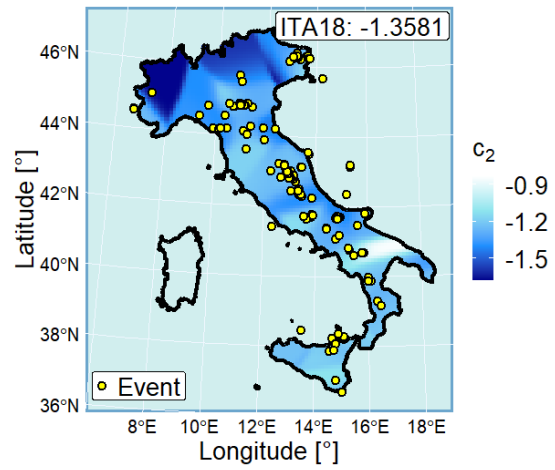


808

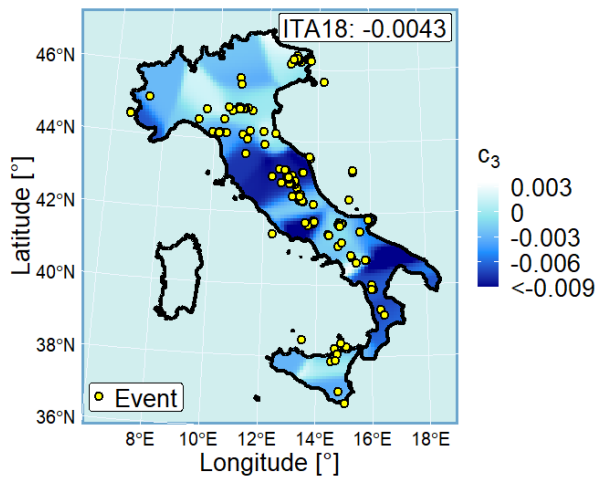
809 **Figure 2.** Stationary coefficients of ITA18 vs ITA18\_MS-GWR: a) offset  $a$ ; b) magnitude scaling  
 810 coefficient  $b_1$ ; c) magnitude scaling coefficient  $b_2$ ; d) strike-slip coefficient  $f_1$ ; e) thrust fault  
 811 coefficient  $f_2$ ; f) magnitude-dependent geometrical spreading coefficient  $c_1$ .  
 812



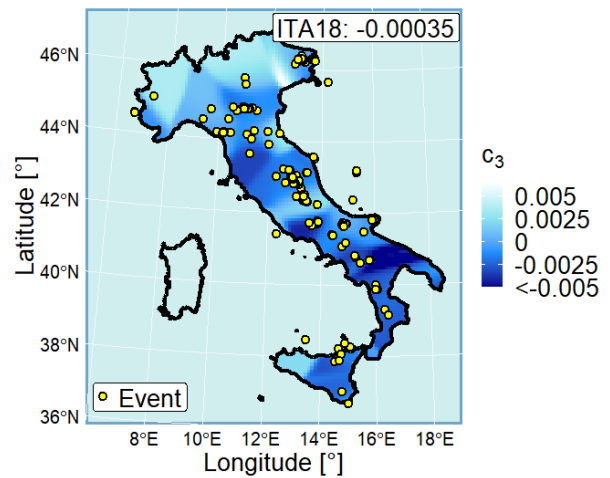
(a)



(b)

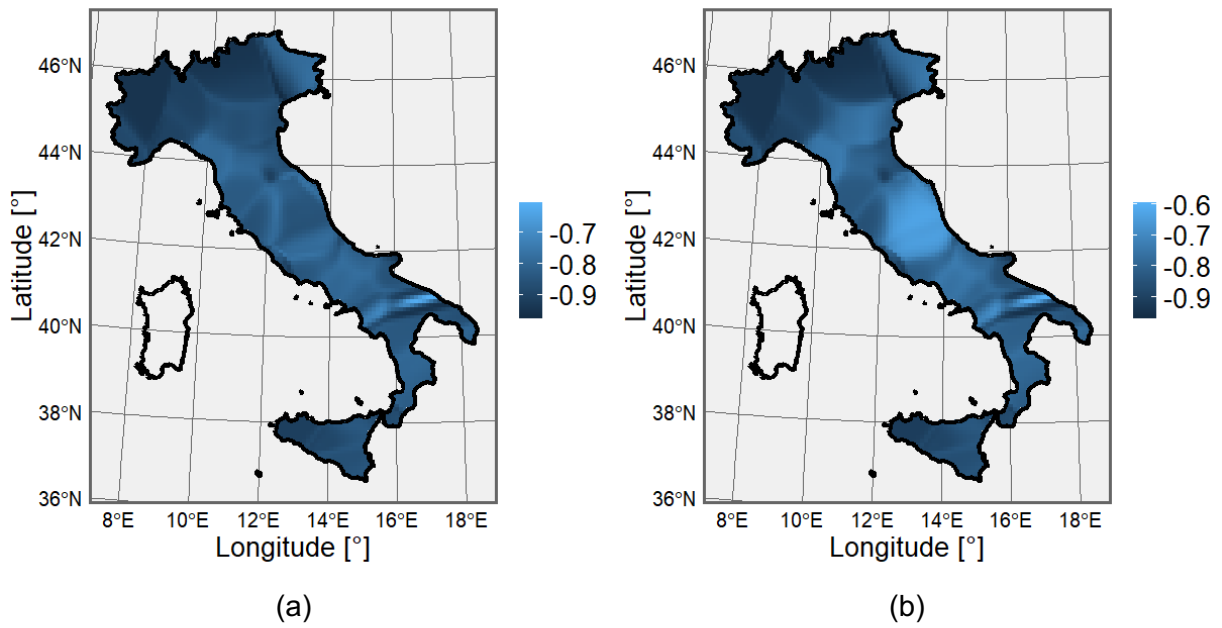


(c)



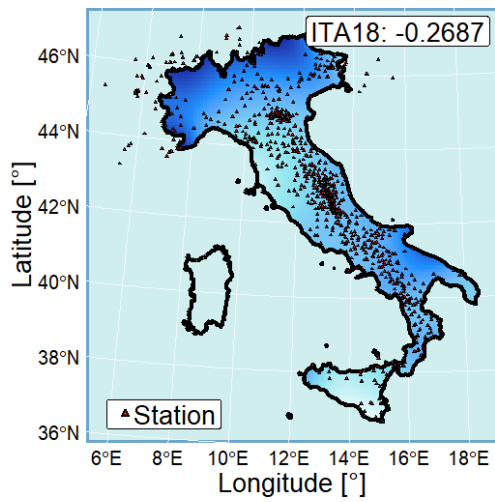
(d)

813 **Figure 3.** Maps of the spatially variable coefficients for the distance scaling: a) geometrical  
 814 spreading coefficient  $c_2$  for SA-T=0.1s; b) geometrical spreading coefficient  $c_2$  for SA-T=1s; c)  
 815 anelastic attenuation coefficient  $c_3$  for SA-T=0.1s; d) anelastic attenuation coefficient  $c_3$  for SA-  
 816 T=1s. The values of stationary coefficients obtained by ITA18 calibration are given in the plot.  
 817

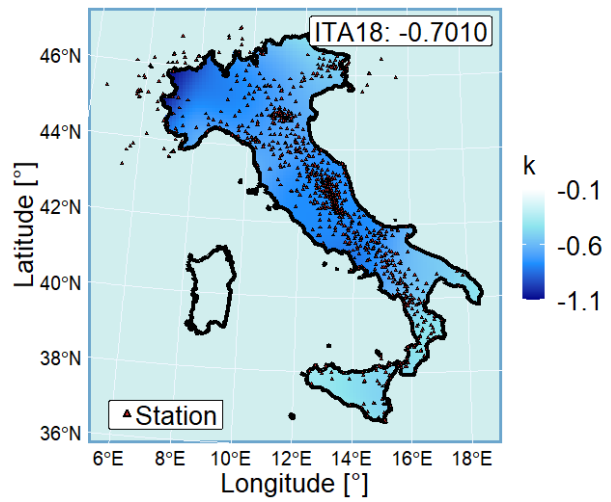


818 **Figure 4.** Maps of the Pearson correlation index between  $c_2$  and  $c_3$  coefficients ( $\rho_{c_2,c_3}$ ): a) SA  
 819 T=0.1s; b) SA T=1s.

820



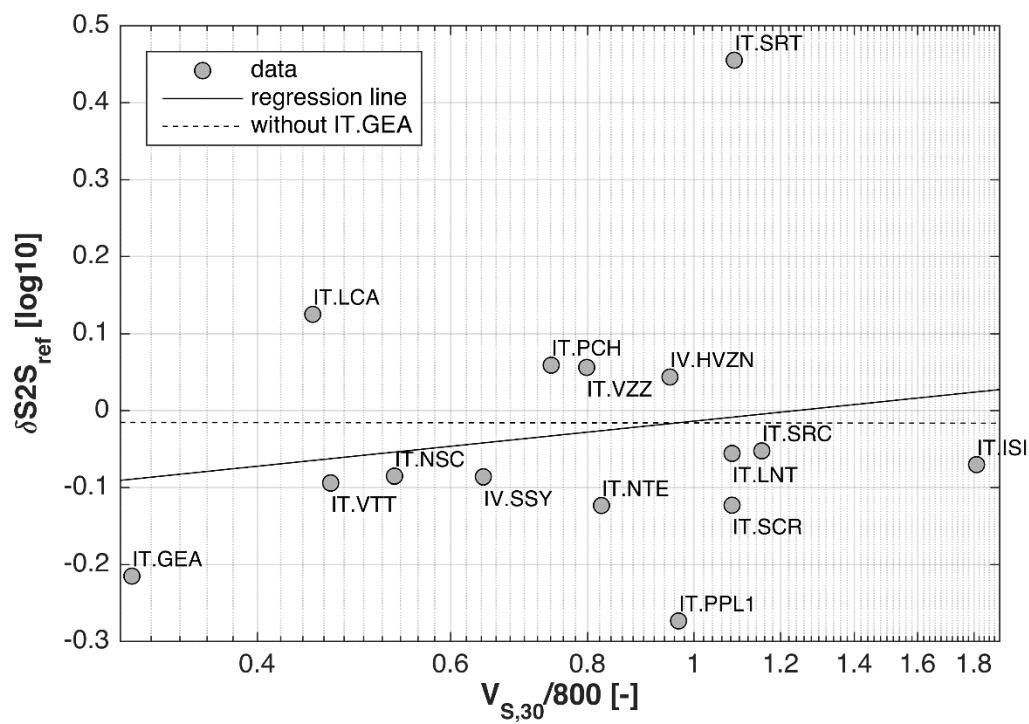
(a)



(b)

821  
822  
823  
824  
825

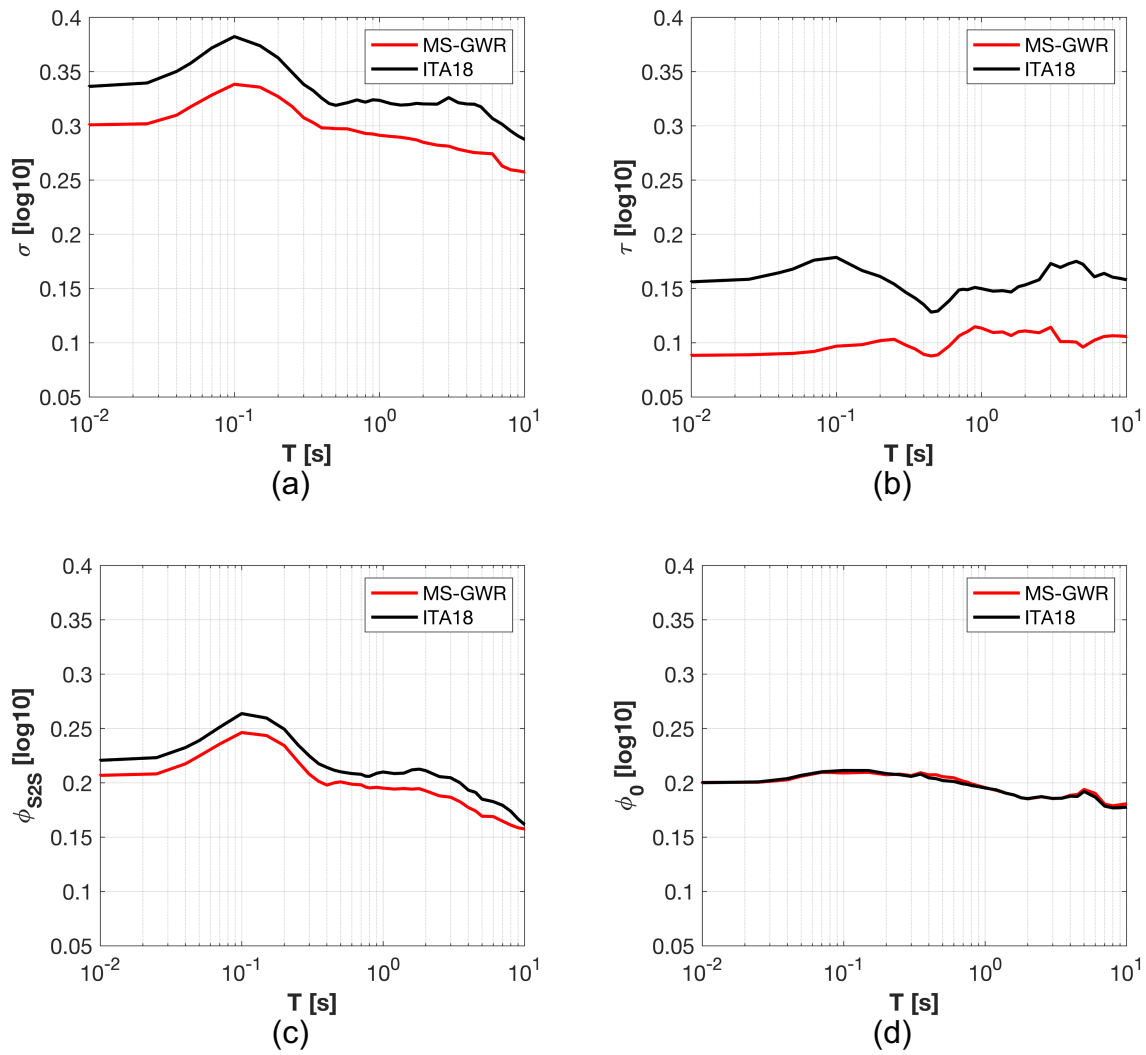
**Figure 5.** Maps of the spatially variable coefficients for  $V_{s,30}$  scaling coefficient  $k$  at: a) SA-T=0.1s; b) SA-T=1s. The values of stationary coefficients obtained by ITA18 calibration are given in the plot.



826  
827  
828  
829  
830

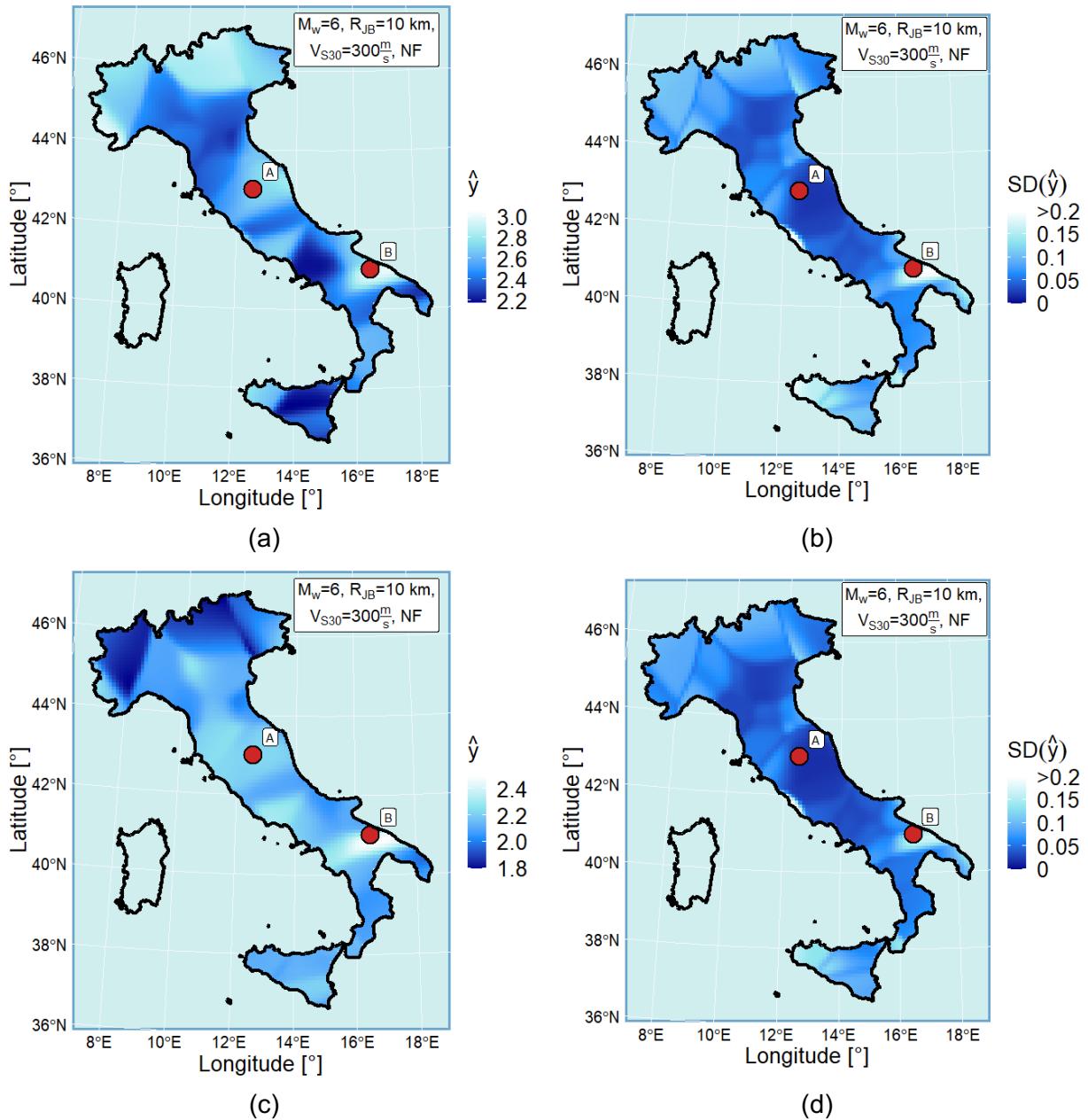
**Figure 6.** Mean site amplification ( $\delta S2S_{ref}$ ) with respect to ITA18 predictions at  $V_{s,30}=800\text{m/s}$  as a function of  $V_{s,30}/800$  for selected station in south-eastern Sicily.



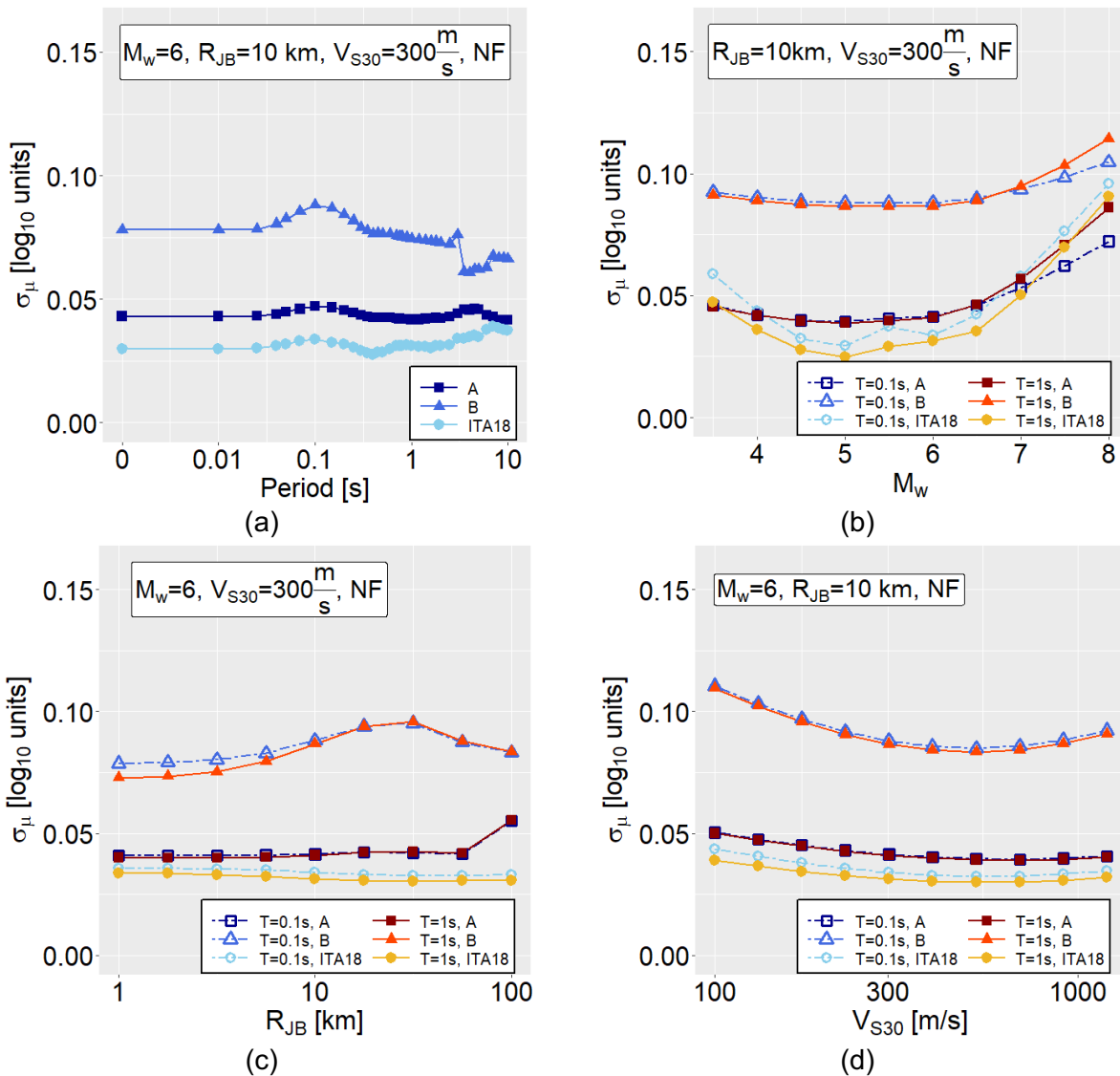


832 **Figure 7.** Standard deviation components vs. period: a) total ( $\sigma$ ); b) between-event ( $\tau$ ); c) site-to-  
 833 site ( $\phi_{s2s}$ ); d) event- and site- corrected residuals ( $\phi_0$ ).

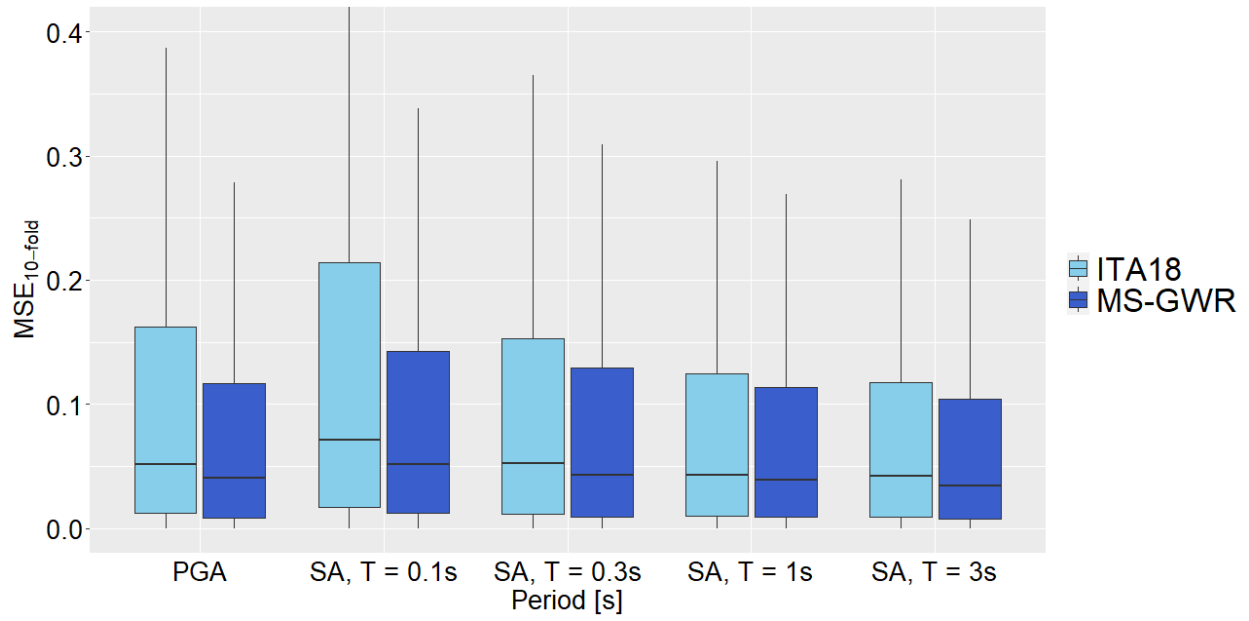
834



835 **Figure 8.** Maps of the median predictions  $\hat{y}$  and associated epistemic uncertainty  $SD(\hat{y})$  for the  
 836 scenario  $M_w=6.0$ ,  $R_{JB}=10\text{km}$ ,  $V_{S,30}=300\text{m/s}$  and normal faults: a)  $\hat{y}$  of  $\log_{10}SA$  at  $T=0.1\text{s}$ ; b)  $SD(\hat{y})$   
 837 of  $\log_{10}SA$  at  $T=0.1\text{s}$ ; c)  $\hat{y}$  of  $\log_{10}SA$  at  $T=1\text{s}$ ; d)  $SD(\hat{y})$  of  $\log_{10}SA$  at  $T=1\text{s}$ .  
 838



840 **Figure 9.** Epistemic uncertainty of MS-GWR model and ITA18 as a function of the predictive  
 841 variables for the sites A and B in Figure 6: a) period; b) moment magnitude  $M_w$ ; c) Joyner-Boore  
 842 distance  $R_{JB}$ ; d)  $V_{S,30}$ .  
 843



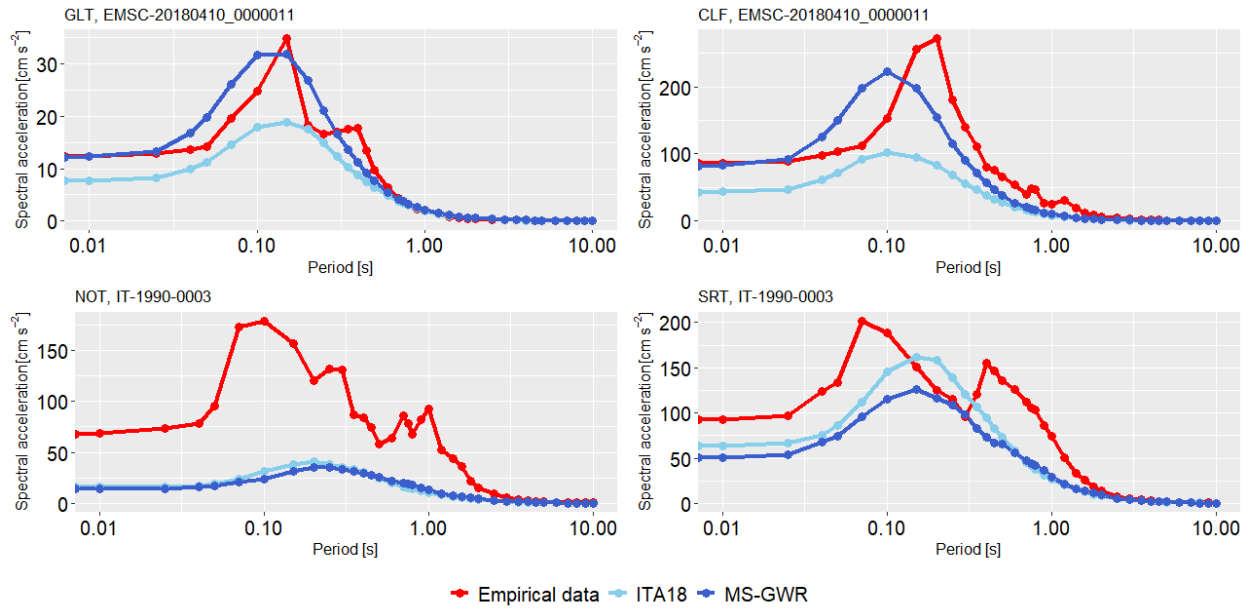
844

845

846

847

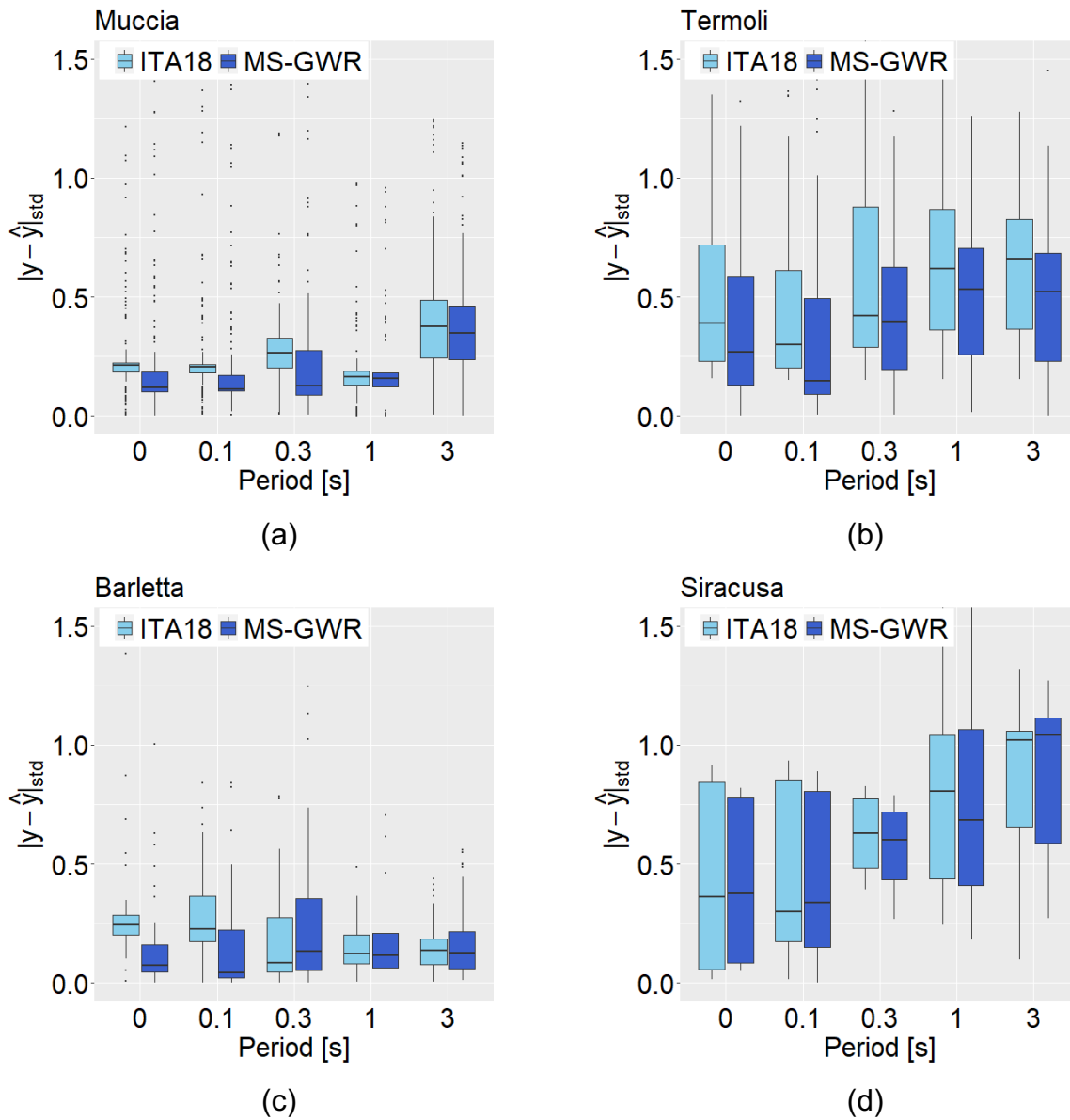
**Figure 10.** Boxplot of MSE by 10-fold cross validation at several periods: comparison between ITA18 model (light-colored error bars) and MS-GWR model (dark-colored error bars).



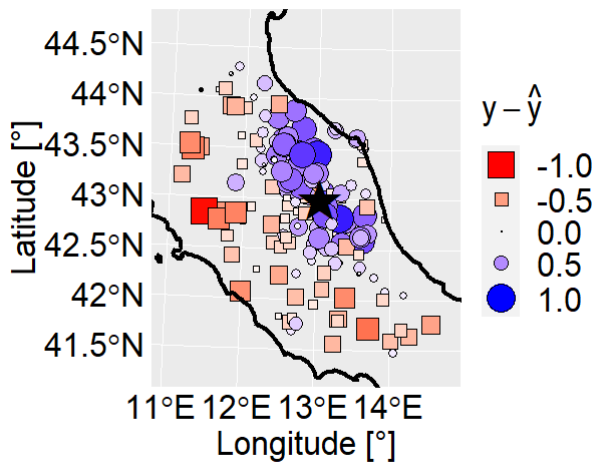
848

849 **Figure 11.** Observed vs predicted spectra.

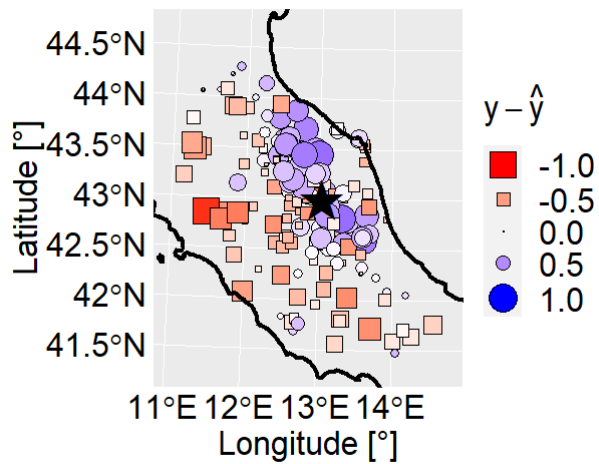
850



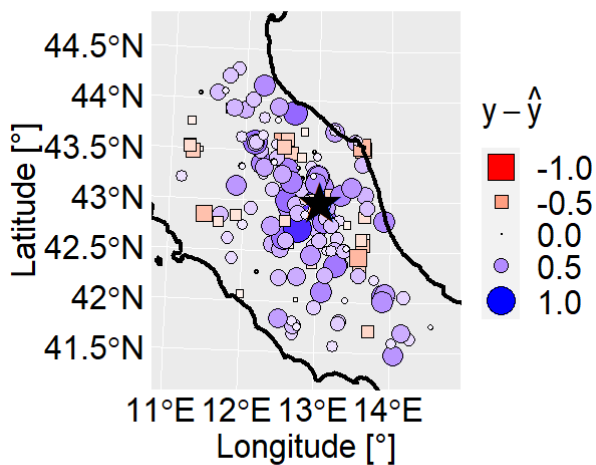
852 **Figure 12.** Boxplot of the standardized residuals for the selected independent events of Table 1:  
 853  $M_w$  4.6 2018/04/10 Muccia (a),  $M_w$  5.1 2018/08/16 Termoli (b),  $M_w$  4.0 2019/05/21 Barletta (c) and  
 854  $M_w$  5.6 1990/12/13 Siracusa (d). The predictions by ITA18 model (light-colored error bars) and  
 855 MS-GWR model (dark-colored error bars) are compared.  
 856



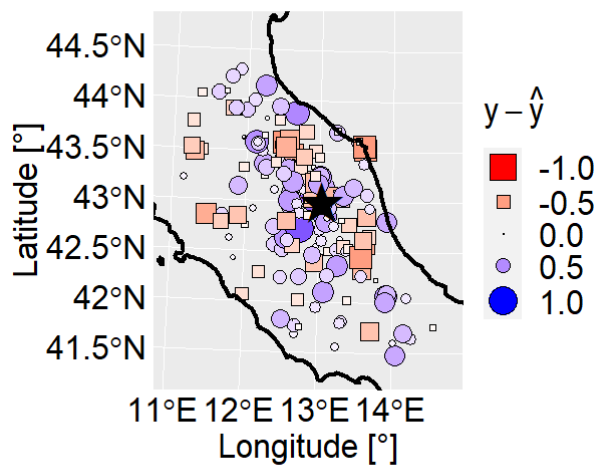
(a)



(b)



(c)



(d)

857 **Figure 13.** Total residuals of the 2018/04/10  $M_w$  4.6 Muccia earthquake: a) ITA18, SA-T=0.1s; b)  
 858 MS-GWR, SA-T=0.1s; c) ITA18, SA-T=1s; d) MS-GWR, SA-T=1s.  
 859